The Binalud Mountains: A key piece for the geodynamic puzzle of NE Iran

Esmaeil Shabanian, Olivier Bellier, Lionel Siame, Mohammad R. Abbassi, D.L. Bourles, Regis Braucher, Yassaman Farbod

The Binalud Mountains: A key piece for the geodynamic puzzle of NE Iran

Esmaeil Shabanian,[1] Olivier Bellier,[1] Lionel Siame,[1] Mohammad R. Abbassi,[2] Didier Bourlès,[1] Régis Braucher,[1] and Yassaman Farbod[1]

Received 22 June 2012; revised 5 October 2012; accepted 16 October 2012; published 28 November 2012.

[1] We applied a combined approach of morphotectonic analyzes of SPOT-5 satellite images and field surveys complemented by in situ-produced ^{10}Be exposure dating to determine the kinematics and rate of active faulting in the Binalud Mountains bounded by the Neyshabur Fault System to the southwest and the Mashhad Fault Zone to the northeast. Three regional episodes of alluvial surface abandonment were dated at ~4.8 ka (Q_1), ~105 ka (Q_3), and ~255 ka (S_3). Along the Neyshabur Fault System, cumulative offsets recorded by Q_3 fan surfaces yield slip rates of 2.4 ± 0.5 and 2.8 ± 0.6 mm/yr for right-lateral and reverse components of active faulting (corresponding to an oblique slip rate of 3.6 ± 1.0 mm/yr), respectively. Reconstructing the cumulative right-lateral offset recorded by S_3 surfaces, a maximum slip rate of 1.3 ± 0.1 mm/yr is suggested for the Mashhad Fault Zone. These imply an overall rate of 3.7 ± 0.6 mm/yr for the range-parallel displacement and an uplift rate of ~2.8 mm/yr due to the range-normal shortening (1.6–2.2 mm/yr) during late Quaternary. The Binalud Mountains are deformed as a soft-linked restraining relay zone, taking up the motion between central Iran and Eurasia at a rate of 4.0 ± 1.3 mm/yr; this translates central Iran in the ~N340°E direction. Our data favor localized faulting, instead of distributed deformation, at the northeastern boundary of the Arabia-Eurasia collision zone.

Citation: Shabanian, E., O. Bellier, L. Siame, M. R. Abbassi, D. Bourlès, R. Braucher, and Y. Farbod (2012), The Binalud Mountains: A key piece for the geodynamic puzzle of NE Iran, *Tectonics*, *31*, TC6003, doi:10.1029/2012TC003183.

1. Introduction

[2] The northeastern part of the Arabia-Eurasia collision zone lies in NE Iran. In that region, active deformation is principally accommodated by active faulting within the Kopeh Dagh [e.g., *Tchalenko*, 1975; *Shabanian et al.*, 2009a] and Binalud mountains (Figure 1), which are structurally connected by the Meshkan Transfer Zone [*Shabanian et al.*, 2009b]. At the longitude of the Binalud Mountains, the Arabia–Eurasia convergence is estimated at 26 ± 2 mm/yr [*Sella et al.*, 2002; *McClusky et al.*, 2003; *Vernant et al.*, 2004; *Reilinger et al.*, 2006]. In eastern Iran, this plate motion results in right-lateral shear on major N–S strike-slip fault systems on both sides of the Lut Block [*Tirrul et al.*, 1983; *Regard et al.*, 2004; *Walker and Jackson*, 2004; *Meyer and Le Dortz*, 2007], where GPS measurements indicate a dextral shear rate of 7 ± 2 mm/yr [*Vernant et al.*, 2004; *Tavakoli*, 2007]. Farther north, in northeast Iran, the available geodetic data [*Vernant et al.*, 2004; *Masson et al.*, 2007; *Tavakoli*, 2007] indicate a convergence rate of 6 ± 2 mm/yr, consistent with the 8 ± 2 mm/yr N-S component of geological slip rate estimate across Kopeh Dagh [*Shabanian et al.*, 2009a]. The similar rates at both the eastern and northeastern boundaries of central Iran implies that the majority of northward motion is transferred from the eastern (e.g., Sistan Fault System) to the northeastern (e.g., Bakharden-Quchan Fault System) boundaries (Figure 1).

[3] *Shabanian et al.* [2009a, 2009b, 2010], *Siame et al.* [2009], and *Hollingsworth et al.* [2006, 2010] present successive discussions on the distribution of active faults and kinematics of deformation in northeast Iran. For the Kopeh Dagh, *Shabanian et al.* [2009a] showed that the northward motion of central Iran relative to Eurasia is principally accommodated by strike-slip faulting (6 ± 2 mm/yr geological rate) localized along the Bakharden-Quchan Fault System (Figure 1). Part (≥25%) of this strike-slip faulting is transferred south through the Meshkan Transfer Zone (Figure 1) [*Shabanian et al.*, 2009b].

[4] Two different tectonic models [*Shabanian et al.*, 2009b; *Hollingsworth et al.*, 2010] are proposed to explain regional tectonic deformation in NE Iran. *Hollingsworth et al.* [2010] suggest that the northward motion of central Iran relative to Eurasia is taken up by (1) range-normal shortening and range-parallel extension in the Kopeh Dagh, accompanied with systematic block rotations around vertical

[1]CEREGE, Aix-Marseille Université, CNRS UM 34, Aix-en-Provence, France.
[2]International Institute of Earthquake Engineering and Seismology, Tehran, Iran.

Corresponding author: E. Shabanian, CEREGE, Aix-Marseille Université, CNRS UM 34, FR-13545 Aix-en-Provence CEDEX 4, France. (shabanian@cerege.fr)

0278-7407/12/2012TC003183

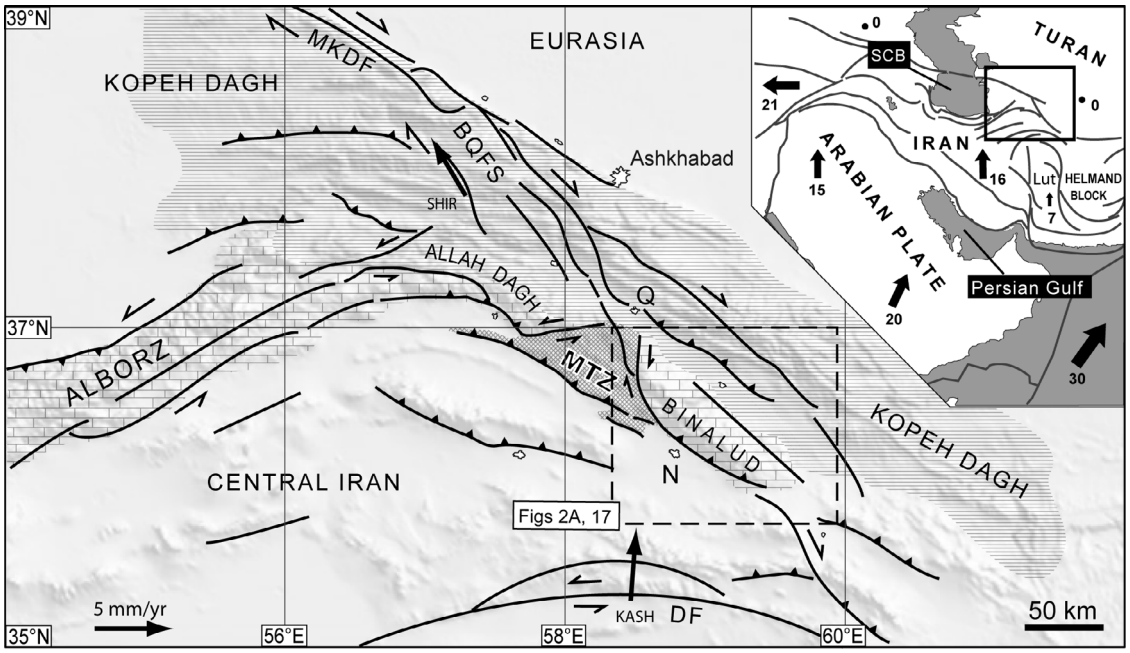

Figure 1. GTOPO30 topographic image showing the regional tectonic setting and major active faults (modified after *Shabanian et al.* [2009b]) of NE Iran. Black arrows are GPS horizontal velocities (mm/yr) in a Eurasia-fixed reference frame [*Masson et al.*, 2007]. The box in the inset shows the location in the Arabia-Eurasia collision framework. Black arrows and associated numbers represent Arabia-Eurasia plate velocities (mm/yr) after *Reilinger et al.* [2006]. Abbreviations: MKDF, Main Kopeh Dagh Fault; BQFS, Bakharden-Quchan Fault System; DF, Doruneh Fault; MTZ, Meshkan Transfer Zone; N, Neyshabur; Q, Quchan; SCB, South Caspian Basin.

axes, and (2) minor thrust faulting in the Binalud Mountains. In contrast, *Shabanian et al.* [2009b] indicate that the deformation is mainly accommodated by strike-slip faulting localized along crustal-scale fault systems that translate central Iran northwestward with respect to Eurasia. Deformation in and near the Binalud Mountains is important in this model. Geologically determined rates and kinematics of the Binalud active faults are partly documented by *Hollingsworth et al.* [2010] suggesting a small contribution (1–2 mm/yr) from these faults to the regional deformation. Our knowledge of present-day deformation field of this region comes from short-term GPS studies [*Masson et al.*, 2007; *Tavakoli*, 2007], which indicate range-parallel right-lateral shear of 2 to 4 mm/yr. This cannot be easily explained by nearly pure thrust faulting on the range-bounding faults, especially on the SW side, as inferred by *Alavi* [1992], *Berberian and Yeats* [1999] and *Hollingsworth et al.* [2010]. An improved understanding of the kinematics of the Binalud Mountains is key to (1) a better understanding of regional geodynamics and (2) identifying which tectonic model is most appropriate.

[5] The current study focuses on the Neyshabur Fault System and the Mashhad Fault Zone in order to characterize rate and kinematics of Quaternary faulting that prevails in the Binalud Mountains. A combined approach to tectonic geomorphology analysis using satellite images (Landsat Enhanced Thematic Mapper Plus (ETM+), SPOT-5 and GeoEye©-Google Earth), regional- and site-scale digital topographic data, and field surveys together with in situ-produced ^{10}Be exposure dating of deformed geomorphic surfaces characterizes the kinematics and rate of active faulting. We used SRTM and regional (10 m pixel size, National Cartographic Center, Iran) digital elevation data for the geomorphic analysis of Quaternary surfaces around the Binalud Mountains. The data and results presented here help in understanding the tectonic evolution of northeastern Iran, highlighting the importance of strike-slip faulting in both the structural and geomorphic evolution of deformation zones involved in the collision.

[6] Before this study, range-bounding faults were mapped only on the regional-scale geological maps [e.g., *Aghanabati*, 1986; *Alavi*, 1992; *Berberian and Yeats*, 1999; *Ghaemi et al.*, 1999; *Pourlatifi et al.*, 2001; *Hollingsworth et al.*, 2010], and no consensus about fault nomenclature was available. We establish a unified fault nomenclature in which both the new structural pattern and preexisting fault names are respected.

2. Active Tectonic Setting

[7] The Binalud Mountains are a 130 km long NW trending range that separates central Iran from the eastern Kopeh Dagh (Figure 2a). It is an asymmetric antiformal range [*Alavi*, 1992] characterized by a gently sloping northeast flank versus a steeply sloping southwest flank that is being thrust over the northeastern margin of central Iran. The Binalud Mountains contain geological structures inherited from paleo-Tethys closure (pre-Late Triassic) that underwent Mesozoic to Cenozoic ductile and brittle tectonic deformation stages [e.g., *Alavi*, 1992; *Sheikholeslami and Kouhpeyma*, 2012]. During the Cenozoic, the Binalud Mountains underwent contractional deformation along with the surrounding regions including the Kopeh Dagh and Allah Dagh mountains [e.g., *Shabanian et al.*, 2009b, 2010].

[8] Presently, the Binalud Mountains are bounded by three major fault systems or fault zones: (1) the NW striking Neyshabur

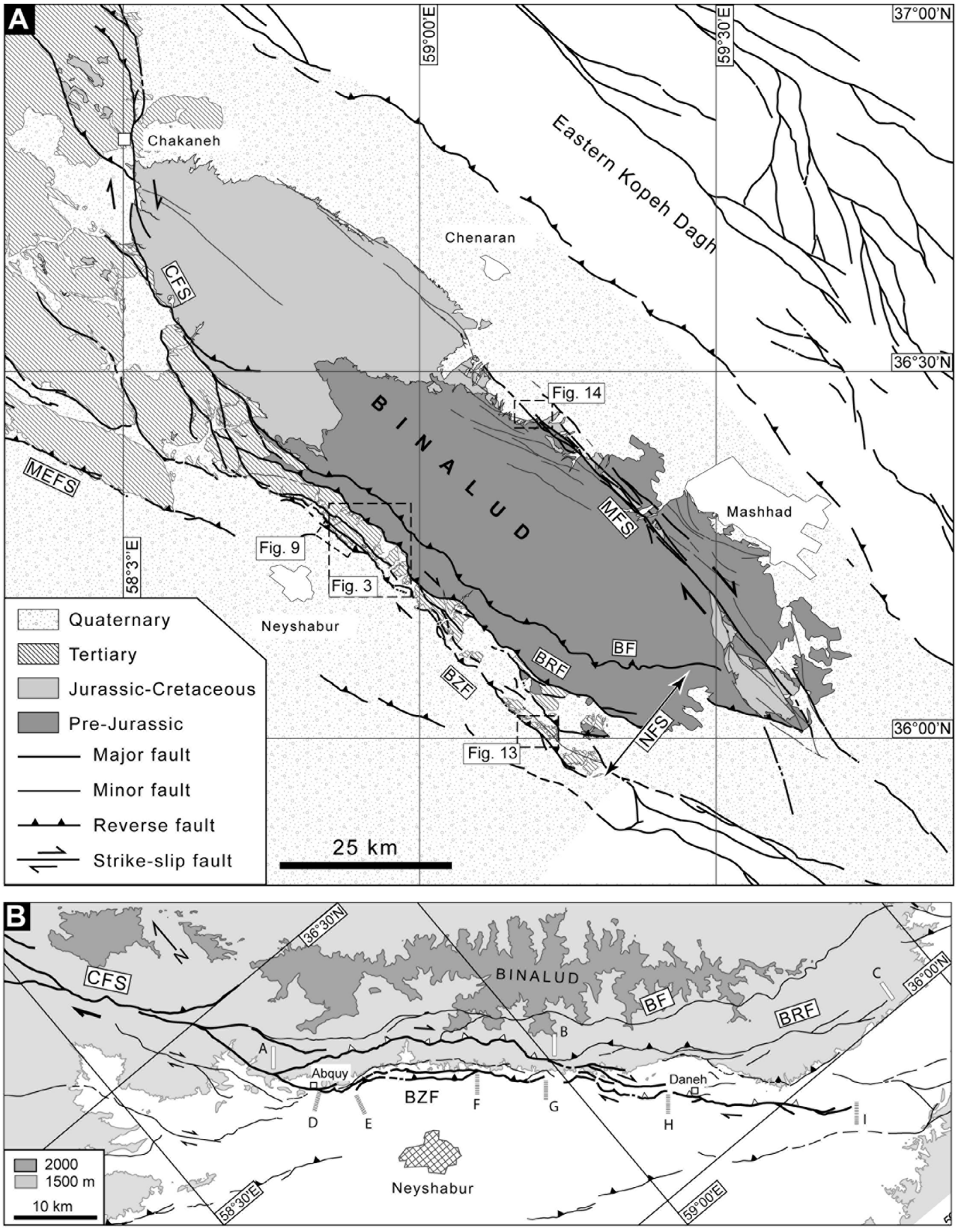
A
59°00'E
59°30'E
37°00'N
36°30'N
36°00'N
58°3°E
Chakaneh
Eastern Kopeh Dagh
Chenaran
CFS
MEFS
BINALUD
MFS
Mashhad
Fig. 14
Fig. 9
Fig. 3
Fig. 13
Neyshabur
BRF
BF
BZF
NFS
Quaternary
Tertiary
Jurassic-Cretaceous
Pre-Jurassic
Major fault
Minor fault
Reverse fault
Strike-slip fault
25 km
B
36°30'N
CFS
BINALUD
BF
BRF
36°00'N
C
A
B
Abquy
Daneh
BZF
D
E
F
G
H
I
2000
1500 m
10 km
Neyshabur
58°30'E
59°00'E

Figure 2

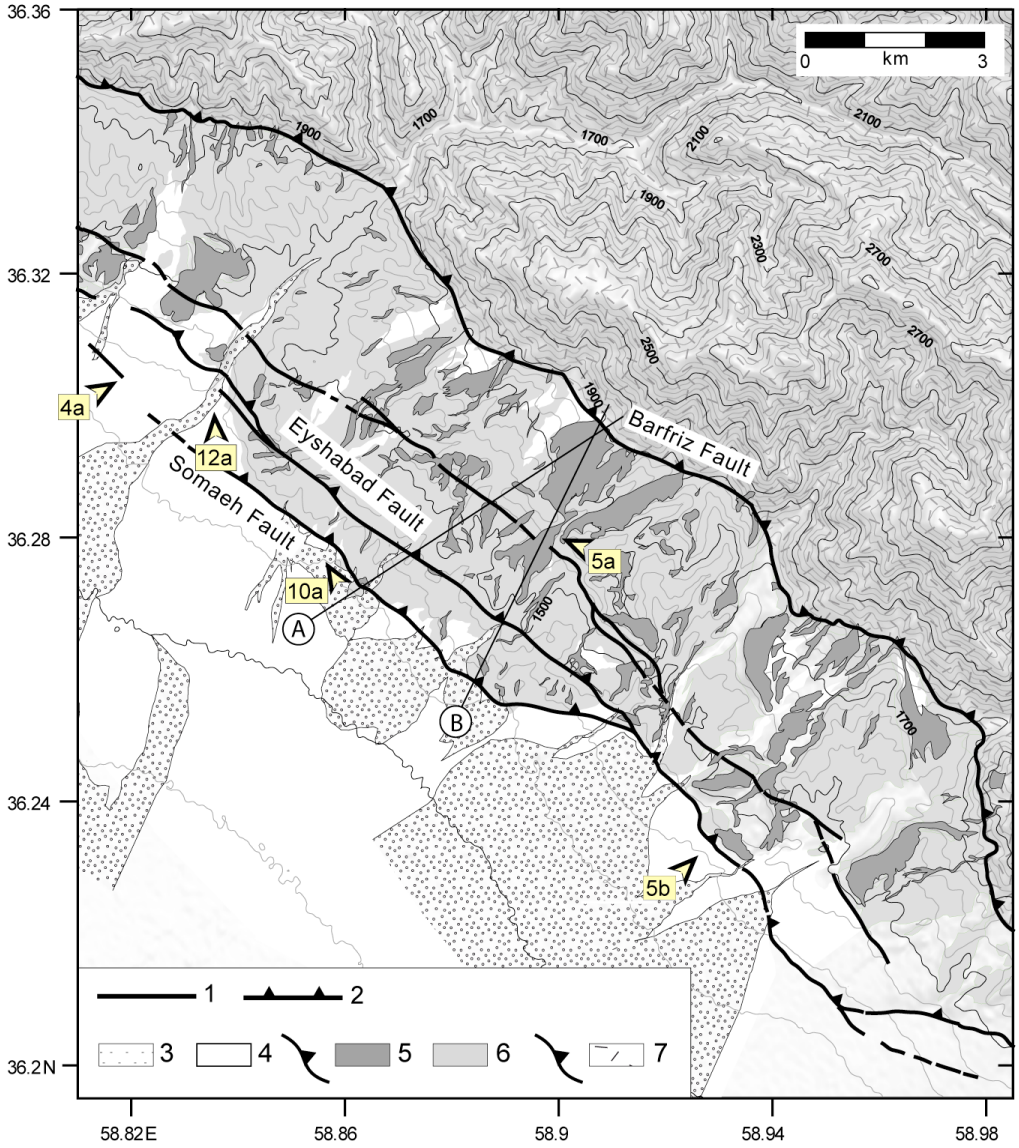

Figure 3. Simplified morphotectonic map of the foothills domain representing major fault segments together with Quaternary alluvial units. Legend: 1, fault; 2, reverse fault (teeth on hanging wall); 3, recent alluvium; 4, undifferentiated Q_1 and Q_2 alluvial deposits; 5, Q_3 fan deposit; 6, Tertiary rock; 7, pre-Cenozoic rock. Topography is shown by 50 m contours interval. A and B show locations of the topographic profiles analyzed in Figure 8. Numbers refer to the location of photographs and their related figure numbers.

Fault System (NFS) to the southwest, (2) the NW striking Mashhad Fault Zone (MFZ) to the northeast, and (3) the north striking right-lateral Chakaneh Fault System (CFS) to the west (Figure 2a).

3. The Foothills Geomorphic Unit

[9] The ~2500 m high Binalud Mountains contrast with a 1.5 to 6 km wide zone of ~1600 m high foothills on the SW side. The foothills are a distinct structural and geomorphic unit between the Barfriz and the Buzhan Fault Zones (Figures 2b, 3, and 4a). We identified three generations of alluvial fans in the foothills, each forming distinct geomorphic abandonment surfaces above active stream beds (from lower to higher and younger to older: Q_1, Q_2 and Q_3 Quaternary surfaces; Figure 3). Q_3 surfaces represent remnants of gently sloping Quaternary alluvial fans (50 to 70 m thick)

Figure 2. (a) Simplified geological map of the Binalud Mountains. Fault traces based on SPOT-5 and Landsat ETM + image mapping [after *Shabanian et al.*, 2009b; this study]. CFS, Chakaneh Fault System; MFS, Mashhad Fault System; NFS, Neyshabur Fault System; MEFS, Meshkan Fault System; BF, Binalud Fault; BRF, Barfriz Fault; BZF, Buzhan Fault Zone. (b) Index map of the Neyshabur Fault System: A–B, northwestern half, and B–C, southeastern half of the Barfriz Fault Zone; D–G, Eyshabad Fault; E–F, Somaeh Fault; B–H, shortcut fault zone; H–I, Qadamgah Fault. Sawteeth mark the hanging wall side of reverse (black) and reverse-dextral (white) faults.

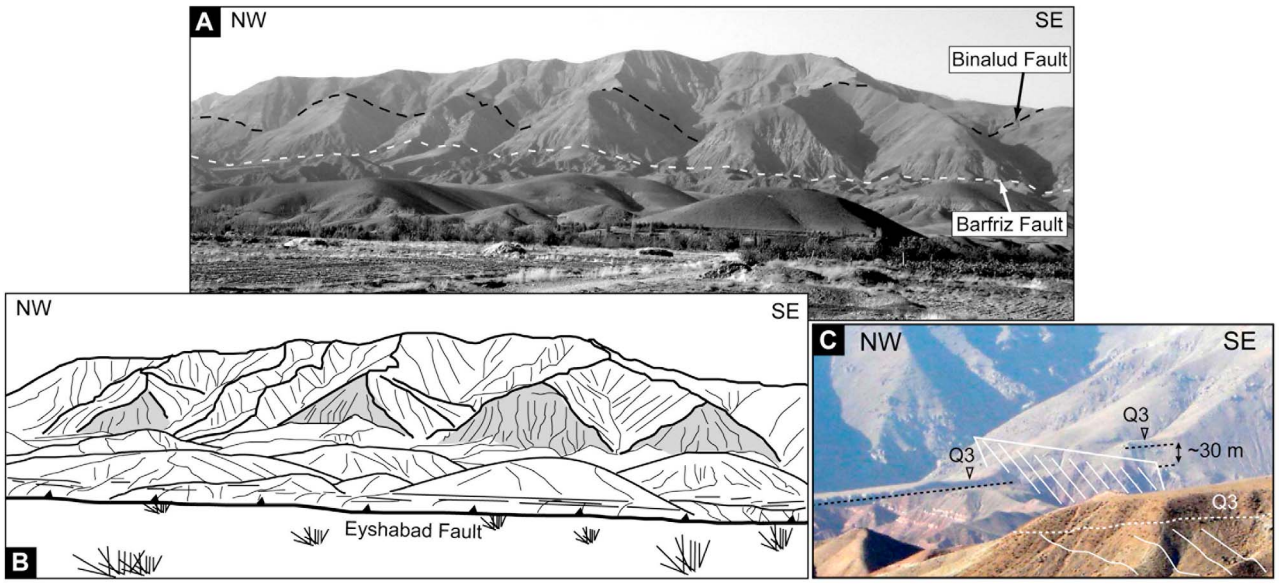

Figure 4. (a and b) General view of the Binalud Mountains taken from ~2 km SW of Eyshabad village showing spectacular triangular facets and different levels of fault scarp lines along the Neyshabur Fault System. The foothills domain is represented by rounded hills between the Barfriz Fault Zone and the Eyshabad Fault. The hills are capped by Q_3 alluvial fans. See Figure 3 for location. (c) Q_3 surfaces are vertically offset across the Barfriz Fault Zone. Location of the photograph is marked in Figure 5b.

overlying folded Tertiary rocks in angular unconformity (Figures 4c and 5). Well preserved Q_3 abandonment surfaces are rare; in most places they are rounded or totally eroded (Figure 5b). The distribution of the Q_3 remnants indicates deposition on an alluvial plain at the front of, and most likely covering, the Barfriz Fault Zone (Figures 3, 5c, and 6c), which marked the Binalud mountain front during deposition of Q_3 unit. The present mountain front, ~4.8 km farther southwest, follows the Buzhan Fault Zone (Figures 2, 3, 5b, and 5c) which bounds the uplifted Q_3 alluvial fans. Lateral and vertical offsets of Q_3 abandonment surfaces (Figures 4c–7) imply late Quaternary activity on the Barfriz Fault Zone.

[10] In the foothills (Figures 2b and 3), intermediate alluvial surfaces (Q_2) are inset within Q_3 alluvial surfaces, and found in narrow patches (15 to 20 m thick) spread along large stream beds. The lower Q_1 geomorphic surface is made of the youngest alluvial fan abandonment surfaces, extending basinward from the Buzhan Fault Zone to the Neyshabur plain (Figure 3). Active streams incise Q_1 fans (~10 m thick) and discharge their deposits downhill from the fault zone to form thin, gently sloping alluvial fans dissipating toward southwest (Figure 3).

4. The Neyshabur Fault System

[11] The Neyshabur Fault System is formed by three nearly parallel, NW striking fault zones (the Binalud Fault, the Buzhan and Barfriz fault zones) running for ~90 km, from the southeastern termination of the strike-slip Chakaneh Fault System (Figure 2). *Aghanabati* [1986], *Alavi* [1992], *Ghaemi et al.* [1999] and *Pourlatifi et al.* [2001] consider the Neyshabur Fault System to be an imbricate thrust fault system inherited from the Mesozoic time, and subsequently reactivated in Pliocene.

[12] Along the NE dipping Binalud Fault, Devonian dolomitic limestones (Bahram Formation) are thrust over Triassic Mashhad phyllites [*Aghanabati*, 1986]. The ~90 km long Binalud Fault was originally a low-angle (~30°) thrust fault associated with mylonite zones indicating ductile behavior at the time of thrusting [*Alavi*, 1992]. The topographic expression of the fault indicates that the fault plane is presently steeply dipping (50°–70°). There is no convincing geological and geomorphic evidence of Quaternary activity along the Binalud Fault.

[13] The ~80 km long Barfriz Fault Zone (Figures 2, 3, and 5) was initially a low-angle (20°–40°NE) thrust fault [*Alavi*, 1992] that juxtaposed Triassic Mashhad phyllites with Tertiary deposits [*Aghanabati*, 1986]. At its northwestern end, the Barfriz Fault Zone joins to the Chakaneh Fault System (Figure 2b). To the southeast, the fault ends in a horsetail splay diverging southeast through the piedmont of the range. The northwest half of the fault zone is localized into a 100 m wide fault zone, whereas the SE half is wider (up to 2.5 km) (Figure 2b). The Barfriz Fault Zone was reactivated in the Late Quaternary, causing combined reverse and right-lateral offsets of alluvial terraces and streams incised in Q_3 surfaces (Figures 4b, 4c, 5b, and Figures 6–8).

[14] The 60 km long, 3 km wide, NE dipping Buzhan Fault zone consists of parallel fault segments, with lengths of 10 to 30 km (Figure 2b). Fault-related morphologies, such as fault scarps and offsets recorded by geomorphic markers, become younger toward the southwest. The Buzhan Fault zone is divided into two geomorphically and structurally distinct parts (1) the northwest part consisting the parallel Eyshabad and Somaeh faults (Figures 2b and 3), along which there is conspicuous geomorphic evidence of reverse faulting, and (2) the southeastern part, the Qadamgah Fault (H–I in Figure 2b), which is an oblique-slip fault with a

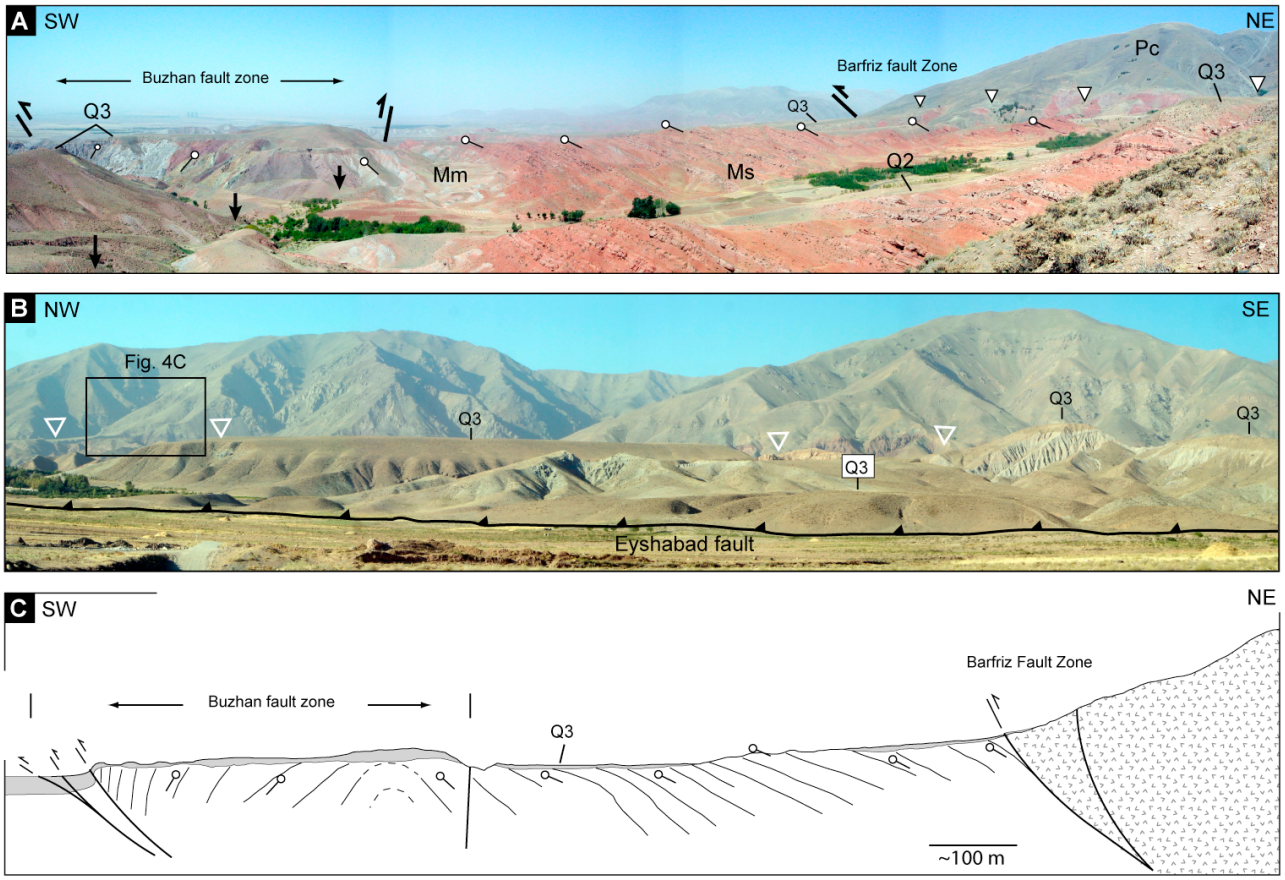

Figure 5. (a) Panoramic view of the foothills domain taken from the Barfriz area (see Figure 3 for the location). Dip of the Miocene strata folded between the Barfriz and Buzhan Fault Zones is indicated. Mm, Miocene marls; Ms, Miocene sandstones. (b) Geomorphic setting of Q_3 surfaces on the hanging wall of the Eyshabad Fault. Trace of the Barfriz Fault Zone is indicated by white triangles. Q_3 within white rectangle shows the Buzhan abandonment surface illustrated in Figure 15b. (c) Schematic structural cross section of the foothills domain principally based on Figure 5a.

prominent right-lateral component of displacement. Such different characteristics suggest along-strike variations in the fault kinematics due to a structural rearrangement within the Neyshabur fault system (see section 4.2.1).

4.1. Morphotectonic Investigations Along the Barfriz Fault Zone

[15] Along the mountain front, triangular facets (Figures 4a and 6c) and Late Quaternary fault scarps (Figure 4c) indicate a significant NE-side up component of slip on the Barfriz Fault Zone. In addition, most streams exhibit systematic deflections or offsets recording a right-lateral component of faulting (Figures 6b and 6c).

[16] Near Barfriz village, a series of Q_3 fan surfaces and their associated streams (Figures 6b and 6c) show geomorphic evidence of both vertical and right-lateral components of faulting along the Barfriz Fault Zone. The right-lateral offsets are expressed in deflected or beheaded streams incised into Q_3 surfaces (Figures 6b and 6c). In some places (Figures 4c, 5b, and 6c), the presence of Q_3 surfaces on both the footwall and hanging wall indicates that (1) the Q_3 alluvial fans were deposited at an inactive mountain front and (2) the late Quaternary reactivation of the fault postdates the abandonment of Q_3 fan surfaces (Figures 4b and 4c). In the Barfriz area, streams with distinct morphology on both sides of the fault have been right-laterally offset (Figure 6). Geomorphic reconstructions of these streams yields a cumulative right-lateral offset of 240 $\pm$ 20 m along the Barfriz Fault Zone (Figure 7).

[17] The reverse component of Quaternary faulting on the NE dipping Barfriz Fault Zone is partly expressed in a SW facing 20 km long fault scarp line (Figure 6) along which Q_3 surfaces are tilted to the SW over a distance of $\sim$150 m downhill from SW of the fault. This tilting is attributed to reverse faulting components on the Neyshabur Fault System with a dominant contribution from the Barfriz Fault Zone. To measure the total vertical deformation recorded by Q_3 surfaces, we have reconstructed the initial morphology of the Q_3 abandonment surface using the undeformed segments of the geomorphic surfaces downhill from the Neyshabur Fault System. The thickness of both Q_1 and Q_2 alluvial fan deposits overlying the downhill Q_3 surfaces does not exceed $\sim$30 m. This value was used to constrain the total vertical displacement (see Figure 8 caption for uncertainties). Two

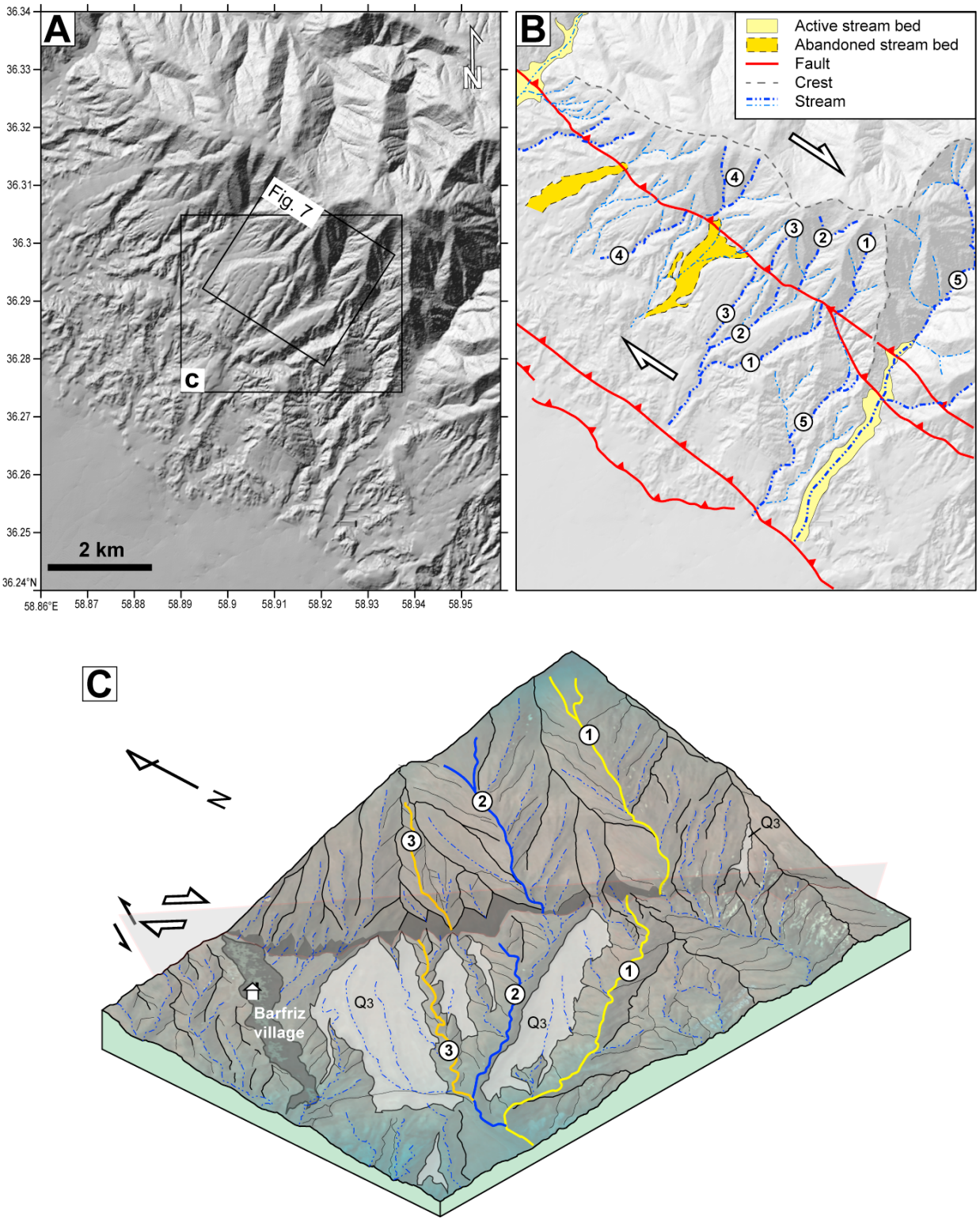

Figure 6. (a) Shaded relief map of the Barfriz area based on 10 m pixel size digital elevation data (National Cartographic Center, Iran). (b) Morphotectonic interpretation of Figure 6a. Streams with "distinct" geomorphology (depth, width and incision pattern) show systematic right-lateral offset/ deflections, crossing the Barfriz Fault. Corresponding stream counterparts are marked by identical numbers. (c) A 3-D view of the Barfriz Fault (GeoEye-GoogleEarth image superposed on 10 m DEM) and its morphotectonic interpretation showing the triangular facets forming a SW facing fault scarp together with streams offset and beheaded along the fault.

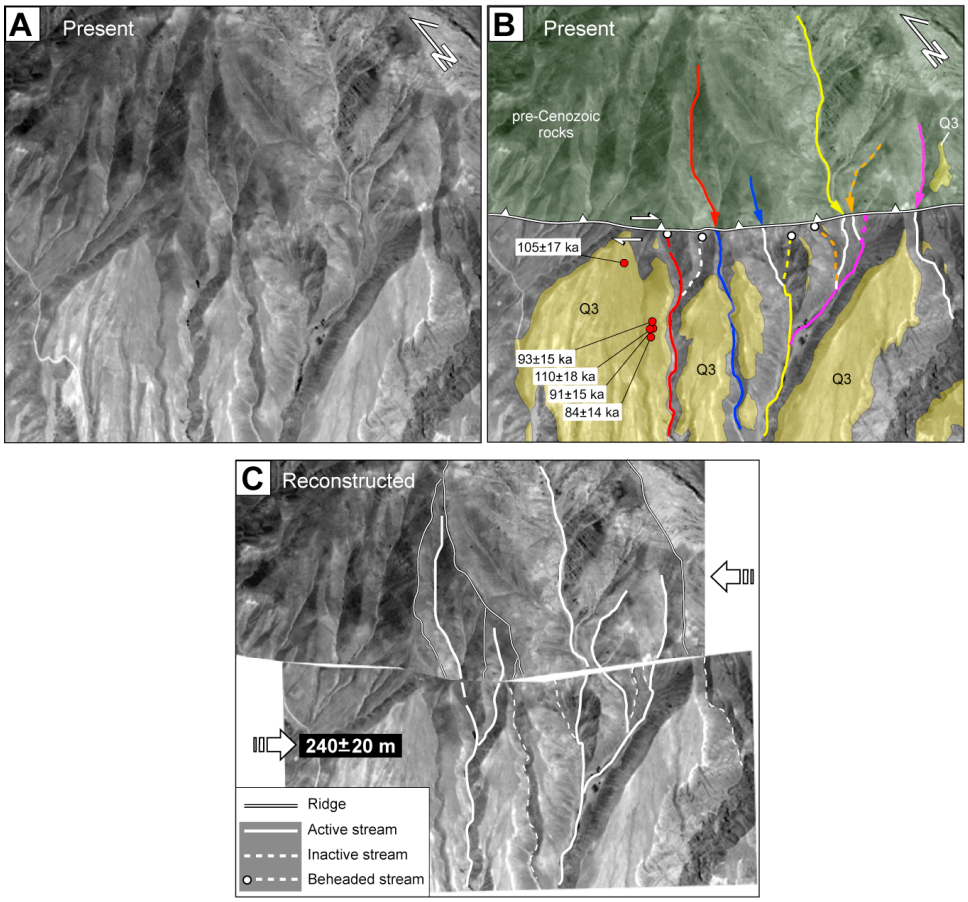

Figure 7. (a) SPOT-5 image centered on the Barfriz Q_3 surfaces and associated drainage systems. (b) Morphotectonic interpretation of Figure 7a. Location and ^{10}Be exposure ages of samples are marked (see Table 1 for more details). Corresponding stream counterparts are shown with the same color. Beheaded streams are marked by circles at the tips. Dashed lines show abandoned streams. (c) Reconstructed geomorphology of the streams and their catchment areas after the restoration of ~240 dextral offset along the Barfriz Fault.

topographic profiles have been analyzed across the Neyshabur Fault System to reconstruct the initial slope of Q_3 surfaces using the equations developed by *Troeh* [1965]. These equations utilize three points of known radial distance from the fan apex to predict the elevation profile of any point along a particular radial line (see *Keller et al.* [2000] for tectonic implications). The reconstructed slope of alluvial fans produced by Troeh's equations was used to estimate vertical deformation postdating abandonment of the Q_3 fan surfaces (Figures 8a and 8b). The change in elevation of the fan apex from the initial position (before the deformation) to its present-day position (after the deformation) implies a cumulative vertical displacement of 290 ± 50 m recorded by Q_3 surfaces (Figures 8a (top) and 8b (top)). This total displacement is accommodated by both the Barfriz and Buzhan Fault Zones (Figure 8). To illustrate contributions of each fault zone, vertical displacements along the profiles were deduced following removal of elevation of the initial fan morphology (Figures 8a (bottom) and 8b (bottom)). For instance, in Figure 8a (bottom), the total 275 ± 35 m post-Q3 vertical displacement across the fault system is divided into a vertical offset of ~140 m across the Buzhan Fault Zone comprising three fault strands, and the remaining ~135 m offset that is attributed to the Barfriz Fault Zone. Analyzing the two profiles (Figures 8a and 8b) a cumulative vertical displacement of 140 ± 50 m is estimated for the Barfriz Fault Zone since the abandonment of Q_3 surfaces.

[18] Our estimates of the reverse (140 ± 50 m) and right-lateral (240 ± 20 m) cumulative offsets imply a total post-Q_3 oblique-slip displacement of 280 ± 100 m along the Barfriz Fault Zone and yield a geomorphically derived plunge angle of ~30°NW for the fault slip vector. The fault trace in both SPOT-5 satellite images and topographic maps, as well as the field data indicate the average geometry of N130°E/60°NE (strike/dip) for the Barfriz Fault Zone. Subsequently, the projection of the ~30°NW plunge angle on the average fault geometry yields a pitch angle of ~34°NW.

4.2. The Buzhan Fault Zone

[19] On the hanging wall of the fault, stratified Miocene marls and sandstones are folded into asymmetric anticlines and synclines trending parallel to the Buzhan Fault Zone (Figures 5a and 5c). The folds have gently dipping northeastern and steeply dipping to overturned southwestern limbs (Figures 5a and 5c) and record contraction of the Tertiary strata between the Barfriz and Buzhan Fault Zones.

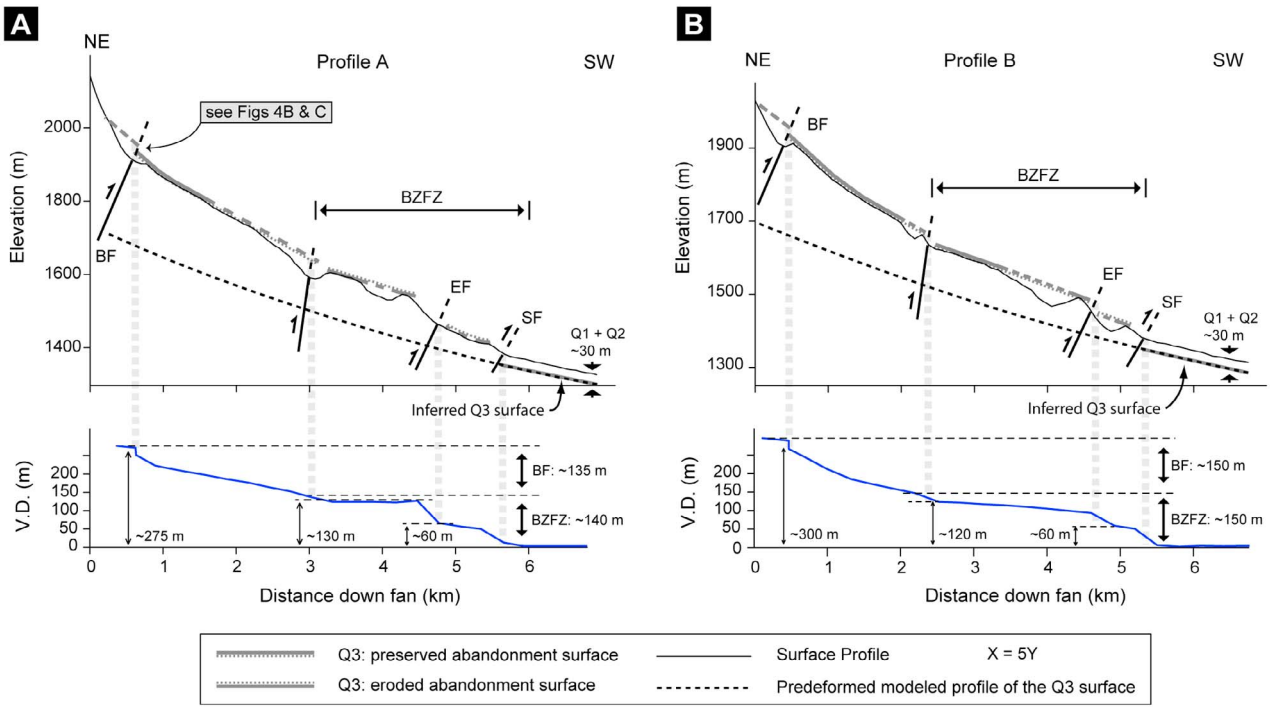

Figure 8. Reconstruction of the initial slope of Q_3 alluvial surfaces using *Troeh* [1965] equations (a) profile A and (b) profile B. (top) Both the initial (black dashed line), and present-day (black solid line) morphology of Q_3 abandonment surface deformed within the Neyshabur Fault System. Thick gray lines are the observed (continuous line) and inferred (dashed line) portions of Q_3. The total thickness of Q_1 and Q_2 alluviums, overlying the Q_3 surface downhill from the fault is estimated at ~30 m. A total uncertainty of 35 m is considered in the measurement of vertical displacements. This incorporates measurement error due to the vertical precision of the topographic data (≤10 m [*Farr et al.*, 2007]) and possible changes in the thickness of Q_1 and Q_2 alluviums (see the text for more information) on the footwall. However, other potential sources of errors could affect our offset measurement. (bottom) Cumulative vertical displacements (blue line) (V.D.) recorded by the Q_3 surface. V.D. represents the difference between the mathematically reconstructed initial (dashed line in Figure 8 (top)) and the deformed (gray line Figure 8 (top)) topographies of Q_3. BF, Barfriz Fault Zone; BZFZ, Buzhan Fault Zone; EF, Eyshabad Fault; SF, Somaeh Fault. For the profile locations see Figure 3.

At the northwest termination of these fault zones, where they join together (Figure 2), the Miocene and Pliocene deposits are folded into an overturned syncline [*Shabanian et al.*, 2009b]. Assuming that stratigraphic ages for the deposits are reliable, the contraction and the consequent folding caused by reverse faulting on the two fault systems should have occurred during or after the Pliocene. Afterward, the erosionally beveled folded rocks were covered by Q_3 alluvial fans, which were in turn affected by the Buzhan Fault zone. Frontal segments of the Buzhan Fault Zone cut through the youngest alluvial fan abandonment surfaces (Q_1) providing evidence of the reverse component of active faulting along the southeast extension of the fault zone (Figures 3, 4a, and 9). These observations indicate the late Quaternary reactivation of preexisting faults within the Buzhan Fault Zone.

4.2.1. Quaternary Fault Offsets Along the Buzhan Fault Zone

[20] Our morphotectonic investigations were conducted at three key sites along the Somaeh, Eyshabad and Qadamgah Faults (Figure 2a). The geomorphic reconstruction of the initial slope of Q_3 surfaces (Figures 8a and 8b) enabled us to estimate a cumulative vertical displacement of 145 ± 35 m on the Buzhan Fault Zone. This cumulative vertical displacement is distributed on three fault strands, with significant contribution of the Eyshabad and Somaeh faults (Figures 8a and 8b). The Eyshabad Fault accounts for 85 ± 30 m of vertical displacement. On the hanging wall of the Somaeh Fault, the Q_3 abandonment surface is not preserved. Thus, a minimum vertical offset of ~60 m is estimated.

4.2.1.1. The Somaeh Fault

[21] The first site is located ~2 km to the north of Somaeh village, near the middle of the Somaeh Fault. The Somaeh Fault is characterized by multiple fault scarps that represent occurrences of several faulting episodes during Late Pleistocene and Holocene time (Figures 9–11). Vertically offset features comprise, at least, three geomorphic terraces, of which the oldest and youngest ones correspond to Q_3 and Q_1 abandonment surfaces, respectively. The youngest geomorphic surface, Q_1 alluvial fans (300 × 400 m in diameter), are cut and offset by the Somaeh Fault (Figure 11b). A man-made channel follows the fault scarp and hides geomorphic details of the fault trace through the Q1 fans. Farther southwest, a surface rupture runs nearly parallel to the main

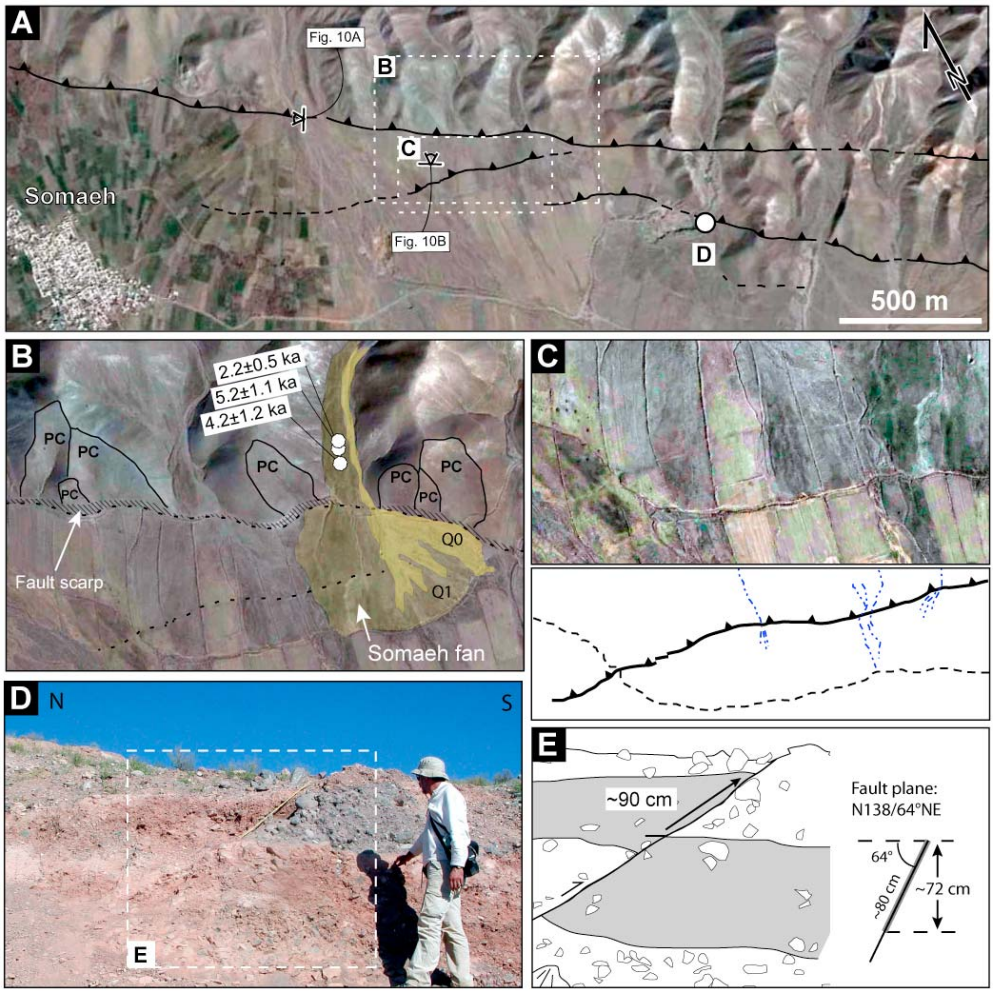

Figure 9. (a) Quickbird image (GoogleEarth) of the Somaeh area. Sawtooth lines are faults. (b) Quickbird image (GoogleEarth) showing the Somaeh fan and catchment areas (PC) uplifted on the hanging wall of the Somaeh Fault. Hatched area shows the ~2.4 m high fault scarp that is clearly visible in the field (see also Figure 10b); sample locations and ages are shown (see Table 1 for sample information). (c) A segment of the rupture along which the vertical offset of ~80 cm is observed; dotted line is a canal. (d) Fault rupture exposed in a quarry (location is marked in Figure 9a). The land surface was slightly modified due to the quarry activity. (e) Field sketch of Figure 9d.

fault trace (Figure 9c). The intermediate age offset features are small (50 × 100 m) drainage basins nested in the southwest face of the fault escarpment, and truncated by the Somaeh Fault (Figures 9b and 10b). The NE parts of these catchment areas uplifted in the fault's hanging wall give the terrace-like appearance (terraced drainage basin) to the landforms (Figures 10a, 10b, and 11a).

[22] Geomorphic analyzes of offset markers (using DGPS-derived digital elevation models) reveal vertical offset values of 2.4 ± 0.2 and 1.3 ± 0.1 m for a "terraced drainage basin" and a Q_1 alluvial fan, respectively (Figure 11). Topographic profiles across the fault rupture indicate a vertical offset of 0.8 ± 0.1 m also recorded by the Q_1 alluvial fan basinward from the main fault trace (Figure 11b). About 2 km to the southeast of Somaeh village, the fault plane was directly observed in a gravel quarry (Figures 9d and 9e). The fault bounds the northeast extension of the quarry and crops out in a NW facing trench wall. A 64°NE dipping fault plane (directly measured in the field) cuts Q_1 alluvium up to the surface and exhibits an apparent offset of 0.90 ± 0.05 m measured on the trench wall (Figures 9d and 9e). The offset value is exaggerated due to the obliquity of ~60°NW sloping trench wall with respect to the fault orientation. By projecting the apparent offset on the actual geometry of fault (N138°/64°NE, Figure 9e) we obtain the dip-slip offset of ~0.80 m, and the vertical throw of ~0.72 m, which is comparable to the geomorphically derived offset of 0.80 ± 0.10 m across the fault rupture (Figure 11b). The lack of convincing structural evidence (e.g., fault striation) precludes an estimate of the lateral component of slip vector.

4.2.1.2. The Eyshabad Fault

[23] Along the Eyshabad Fault, a key site was selected 2.5 km north of the village of Somaeh [*Shabanian*, 2009] (Figure 12). A SW running river crosses the northwestern end of the Eyshabad Fault and incises alluvial surfaces Q_1, Q_2 and Q_3. In the hanging wall of the fault, vertical

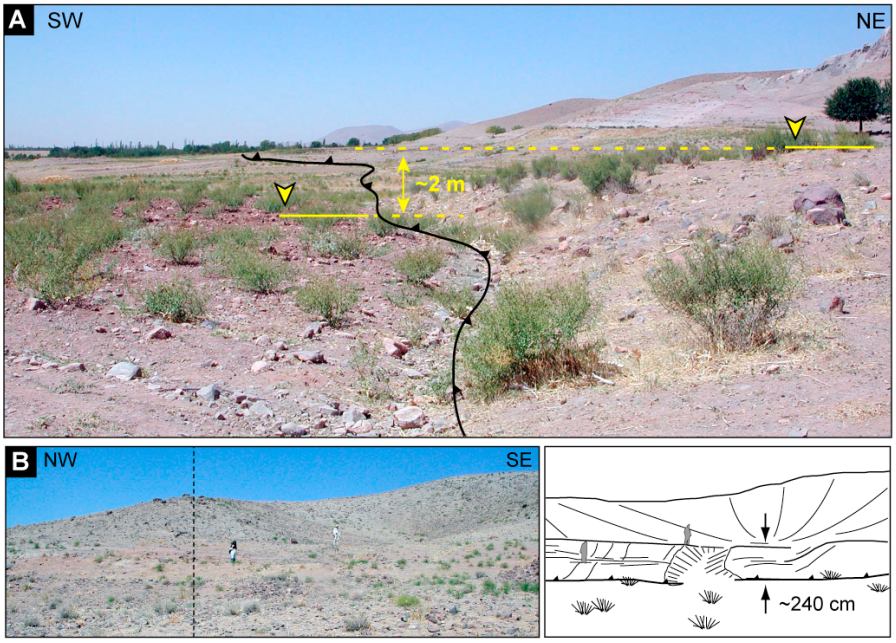

Figure 10. (a) General view of the Somaeh fault scarp north of Somaeh village. (b) Field photograph of the ~2.4 m high multiple fault scarp along the Somaeh Fault. See Figure 9a for location of the field photographs.

downcutting by the river into these surfaces has preserved flights of alluvial terraces perched above the modern river valley. In the NW bank of the river, a spectacular profile of the fault is exposed [see also *Shabanian*, 2009; *Hollingsworth et al.*, 2010] thanks to cut bank erosion. This provided suitable conditions to measure the geometry (N140°E striking, 55°NE dipping) and kinematics of the Eyshabad Fault (Figure 12b). Fault striae measured on the fault plane indicate dominantly reverse kinematics with a minor right-lateral component (pitch angle of 85°NW). In Q_2 alluvial deposits, a cumulative vertical offset of ~15 m was measured in the river bank (Figure 12b).

4.2.1.3. The Qadamgah Fault

[24] Along the Qadamgah Fault (Figures 2b and 13), remnants of Q_3 deposits are preserved at the top of rounded hills on the hanging wall of the fault (NE side) suggesting that the entire area was covered by Q_3 alluvial fans (Figure 13a and 13b). Q_3 surfaces are incised by nearly parallel streams (~3 km long) that flow southwest, perpendicular to the fault trace. These streams are right-laterally deflected and/or offset when they cross the fault (Figures 13b–13d). Some of the hanging wall streams were reconnected to other footwall streams to form new drainage arrangements (Figures 13c and 13d). The geomorphic reconstruction of the affected steams indicates a weighted mean cumulative right-lateral offset of 260 ± 40 m postdating the abandonment of the Q_3 surface (Figures 13b–13d).

[25] The lateral offset on the Qadamgah Fault is consistent with the lateral offset observed on the Barfriz Fault Zone. Such a change in the kinematics of the Buzhan Fault Zone, from reverse to oblique dextral faulting, is explained by a structural linkage between the Qadamgah and Barfriz Faults through which dextral faulting is transferred southeastward. This suggestion seems reasonable when considering the structural complexity in the fault pattern at the central part of the Neyshabur Fault System (Figure 2b, section B–H). At a longitude of 59°E, nearly north striking fault segments form a shortcut zone between the Barfriz and Qadamgah Faults. The shortcut zone (Figure 2b) dissects the foothills domain into two distinct parts. The northwest part comprises Q_3 fan surfaces uplifted and deeply incised in the hanging wall of the Buzhan Fault Zone. Conversely, the southeastern part is covered by Q_3 deposits which form relatively well preserved and slightly deformed surfaces. The shortcut zone explains why the southeastern part of the Barfriz Fault is a reverse fault array, while the northwestern part is a ~100 m wide oblique-slip dextral-reverse fault zone (Figure 2b).

5. Morphotectonic Investigations Along the Mashhad Fault Zone

[26] The ~125 km long Mashhad Fault Zone strikes northwest (Figure 2a) comprising several NW striking fault segments most of which are remnants of the paleo-Tethys suture zone [e.g., *Majidi*, 1978]. The Mashhad Fault Zone is expressed by linear fault traces in the topography [e.g., *Hollingsworth et al.*, 2010]. The lack of significant changes in elevation across these straight fault traces suggests that the fault zone is vertical and likely a network of strike-slip fault strands. North of latitude N36°, several parallel faults extend northwest over a distance of ~40 km from Chenaran town (Figure 2a). Their linear traces in the Mesozoic bedrock exhibit systematic, though ambiguous deflections in drainage systems. Quantitative geomorphic analyses by *Shabanian* [2009] provided indirect evidence of Quaternary activity along these structures. However, it is not yet clear if those faults can be considered as the continuation of the Mashhad Fault Zone.

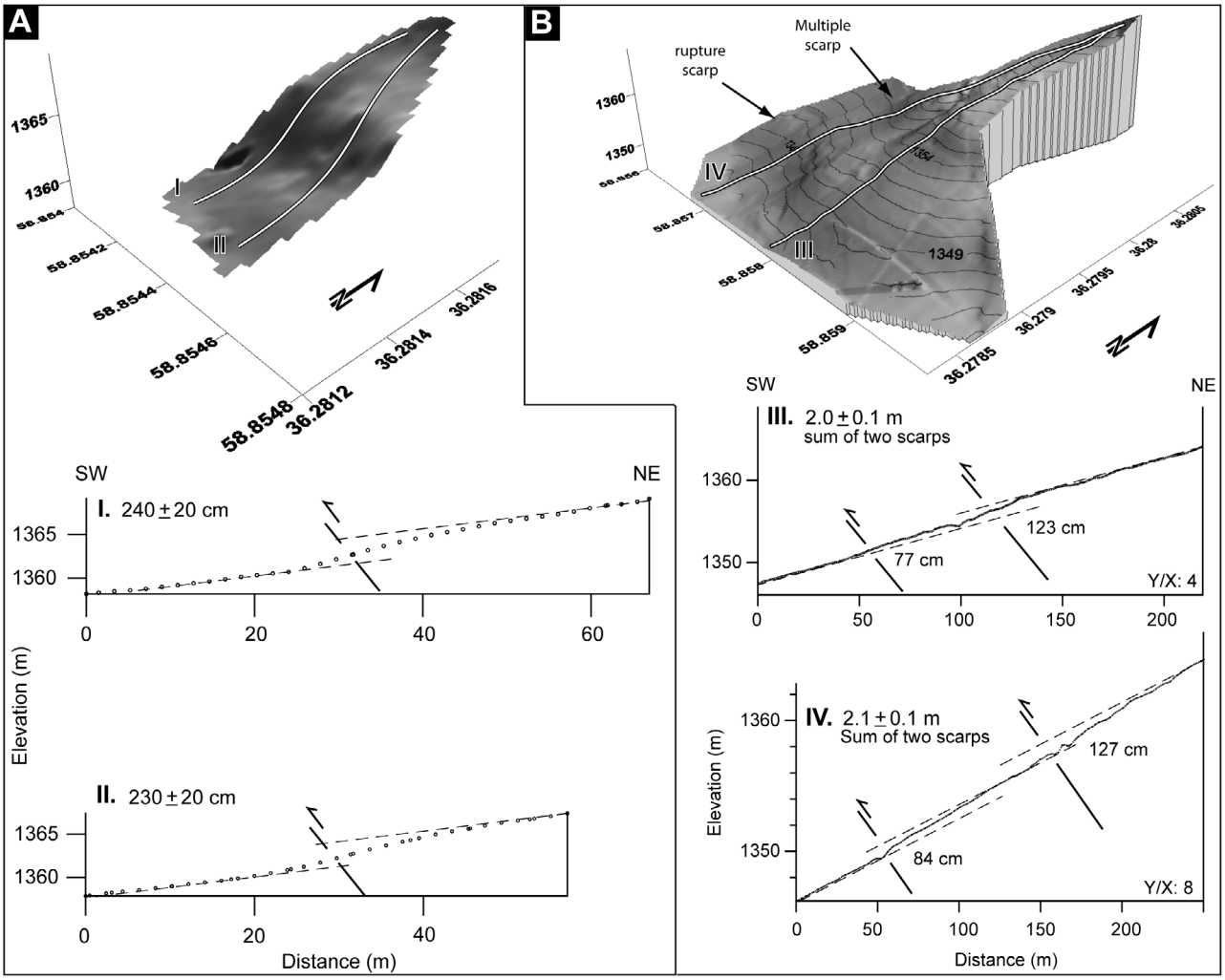

Figure 11. (a) Differential GPS-derived DEM from the ~2.4 m high multiple fault scarp along the Somaeh Fault presented in Figure 10b together with I and II topographic profiles. (b) DGPS-derived DEM of the Somaeh fan accompanied by two topographic profiles which show the cumulative offset of ~1.2 m on the main fault trace and the ~80 cm high scarp.

[27] At the northeast flank of the Binalud Mountains, northwest of Mashhad, three distinct S_1, S_2 and S_3 Quaternary surfaces (from younger to older) can be distinguished. The highest and oldest Quaternary surface (S_3) corresponds to Quaternary alluvial fans uplifted and partly eroded at the piedmont of the Binalud Mountains (Figure 14a). Younger alluvial fans (S_2 and S_1) are inset into S_3 surface and preserved downhill from the fault zone. The Mashhad Fault Zone cuts the S_3 surface and stream channels incised into the surface (Figure 14).

5.1. Cumulative Fault Offsets Along the Mashhad Fault Zone

[28] Along its northwestern section, the Mashhad Fault Zone right-laterally offsets S_3 alluvial fans (Figure 14). Some surfaces are better preserved and less eroded, with white quartzite boulders typically ≤0.50 m in diameter dispersed on the top surface. In that area, key markers were right-laterally offset along the main strand of the Mashhad Fault Zone (Figures 14b and 14c). The remnant of the Kahu alluvial fan southwest of the fault can be correlated to its counterpart (fan toe) on the northeastern fault side (Figure 14b). Farther east, a main stream channel expresses a similar offset. Although the east and west banks are not well preserved, the overall form of the stream shows nearly the same right-lateral offset as the Kahu fan. Several hundred meters southeast of the Kahu alluvial fan, the fault offsets a stream and makes the upstream segment beheaded (Figures 14b and 14c). Subsequently, the downstream segment has used the bed of another stream less developed than the abandoned segment. The geomorphic reconstruction of the offset stream indicates the cumulative right-lateral offset of 340 ± 20 m, which is similarly recorded by the Kahu fan remnant (Figure 14b), postdating the abandonment of the S_3 surfaces.

6. Surface Exposure Dating

[29] We used in situ-produced ^{10}Be cosmogenic nuclides resulting from spallation and muonic reactions on silicon and oxygen in quartz. Since the progress made over the last

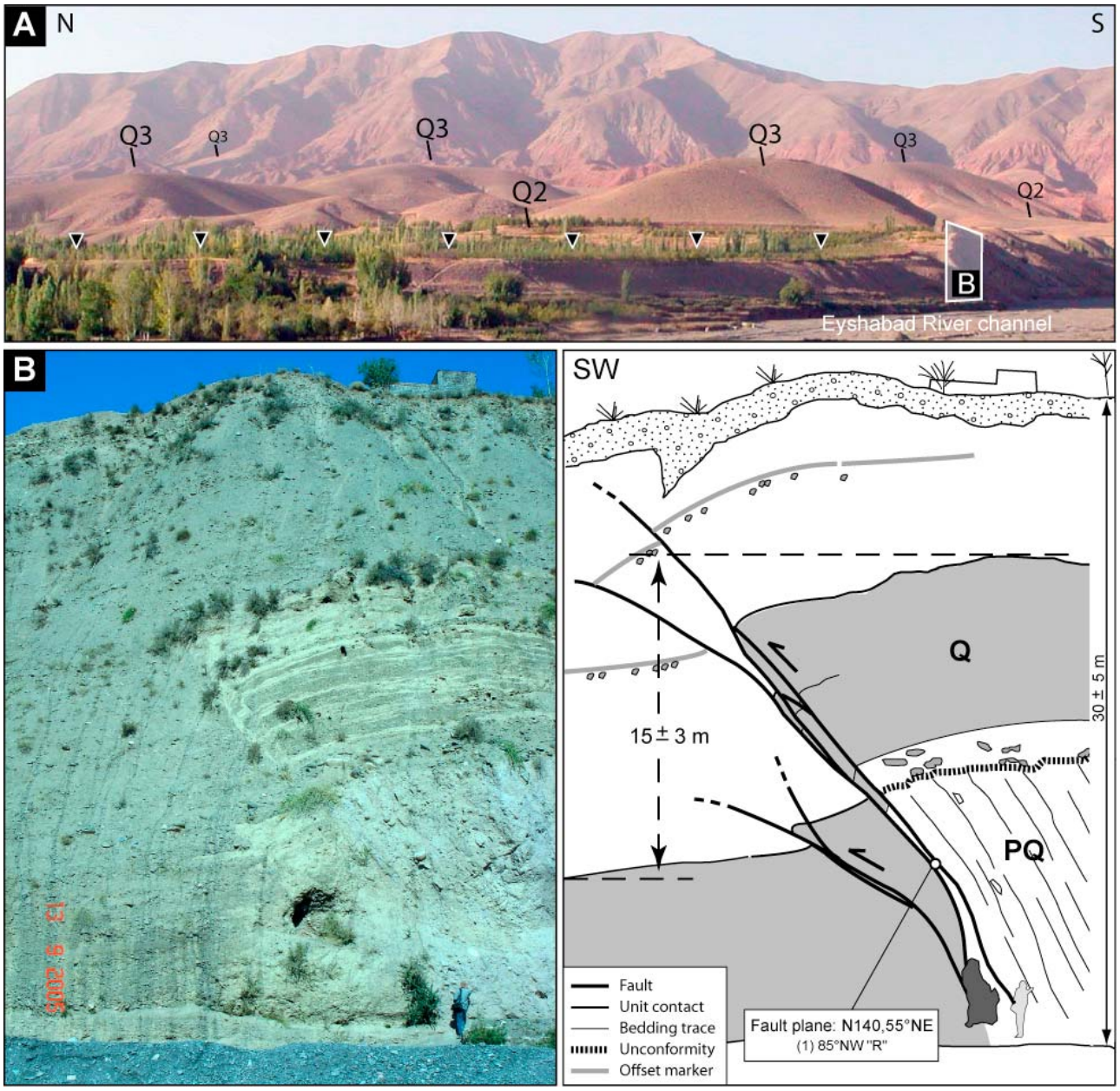

Figure 12. (a) Field photograph showing a general view of the Eyshabad Fault geomorphology; see Figure 3 for the location of the photograph. The main trace of the Eyshabad Fault is marked by black triangles. (b) A natural cross section of the Eyshabad Fault in a river bank north of Eyshabad village; Q, Quaternary; PQ, steeply dipping pre-Quaternary strata. Effects of both image distortion and trench wall slope have been taken into account to estimate the offset value of 15 ± 3 m. Box in Figure 12 (right) shows geometry of the main fault plane; (1) is the pitch angle of the striation measured on the fault plane. "R" means reverse.

decades by the Accelerator Mass Spectrometry (AMS) technique, cosmogenic nuclides are extensively used to date stable geomorphic surfaces (see reviews by *Gosse and Phillips* [2001] and *Dunaï* [2010]).

[30] A total of 16 samples (among 60 samples) collected from quartz-rich boulders of 0.3 (quartzite) to 1.0 m (sandstone and andesite) in diameter were analyzed. The boulders were embedded in flat and pristine parts of four alluvial fan surfaces. The sampled part of the fan surfaces are located away from recent incision rills, and we suggest those did not suffer from overland flows and extensive surface erosion by sheet flows (photographs in Figure 15). Considering the exponential decrease of the in situ-produced ^{10}Be concentrations with depth, boulders showing altered and/or spalled surfaces, angular and visibly broken were avoided and samples were collected from the upper 1–8 cm on top of the boulders.

[31] Cosmogenic ^{10}Be concentrations due to a complex exposure history of clasts, i.e., inheritance, overestimate the true abandonment age of alluvial surfaces [e.g., *Le Dortz*

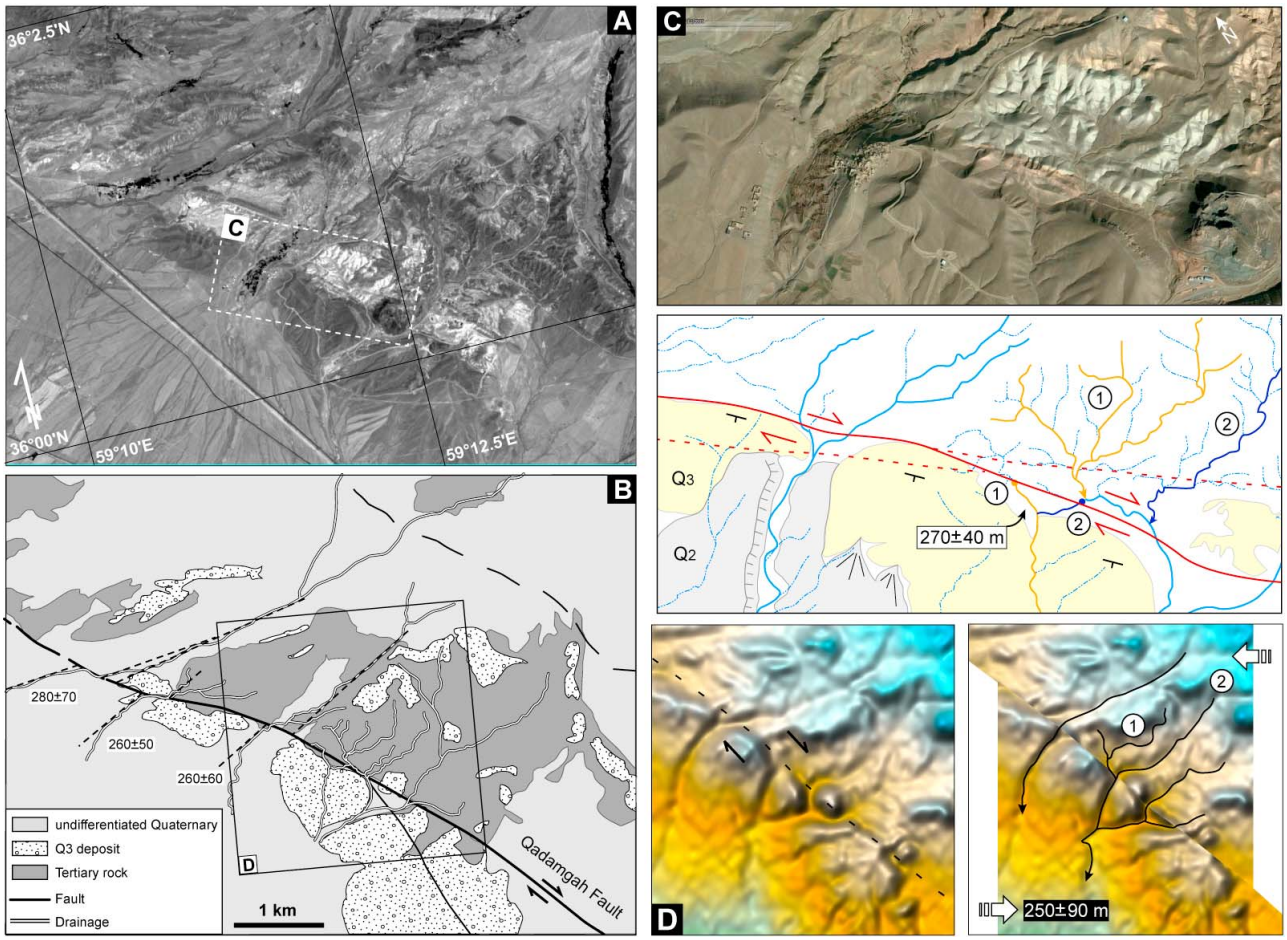

Figure 13. (a) SPOT-5 image centered on the central part of the Qadamgah Fault. (b) Simplified morphotectonic map of the area in Figure13a showing systematic right-lateral offsets/deflections recorded by streams; piercing points are the intersection between dashed lines parallel to the overall trend of steams and the fault trace. Two dashed lines along a stream segment show two offset possibilities. (c) GeoEye image (GoogleEarth) of the area marked in Figure13a together with its morphotectonic interpretation (below). Drainage systems 1 and 2 are disordered due to dextral component of faulting; note two distinct orientations of the axial streams (close to the fault), which correspond well with their counterparts (same color) to the SW. Piercing points are marked by arrow and point of the same color. (d) Geomorphic reconstruction (SRTM shaded image) of three drainage systems (including 1 and 2 in Figure 13c) incised in Q_3. These yield a mean value of 260 $\pm$ 40 m (95% confidence) for dextral offsets. Uncertainties incorporate errors in measurements due to the resolution of images and offset restoration possibilities.

et al., 2011; *Schmidt et al.*, 2011]. Two principal causes of variable inherited ^{10}Be components are different source areas and complex transport histories. Clasts coming from a large catchment area and through a long transport pathway should undergo a complex transport history. This problem would be worse for inset Quaternary terraces, where, clasts are detached from upper alluvial surfaces, and form lower inset terraces downstream [e.g., *Le Dortz et al.*, 2009, 2011; *Schmidt et al.*, 2011; *Le Béon et al.*, 2010; *Ritz et al.*, 2006a]. In Binalud, the source areas of the sampled alluvial fans are rather short (2–20 km) with steep (40°–60°) catchments, implying short transport times and little along-stream storage. Except for one Q_1 alluvial fan (the lowest one), there are no other Quaternary surfaces uphill from the sampled part of the alluvial fans. These particular geomorphic situations minimize inheritance of in situ-produced cosmogenic ^{10}Be in our samples.

[32] Samples were prepared for AMS ^{10}Be measurements following chemical procedures adapted from *Brown et al.* [1991] and *Merchel and Herpers* [1999]. Samples were first crushed and sieved to obtain fraction comprised between 1 and 0.250 mm. After a magnetic separation, the nonmagnetic fraction underwent selective etchings in fluorosilicic (H_2SiF_6) and hydrochloric acids (HCl) to eliminate all mineral phases but quartz. Quartz minerals then were etched in hydrofluoric acid to eliminate potential surface contamination by ^{10}Be produced in the atmosphere. The cleaned quartz grains were then completely dissolved in hydrofluoric acid after addition of $\sim$100 μL of an in-house 3×10^{-3} g/g ^{9}Be carrier solution prepared from deep-mined

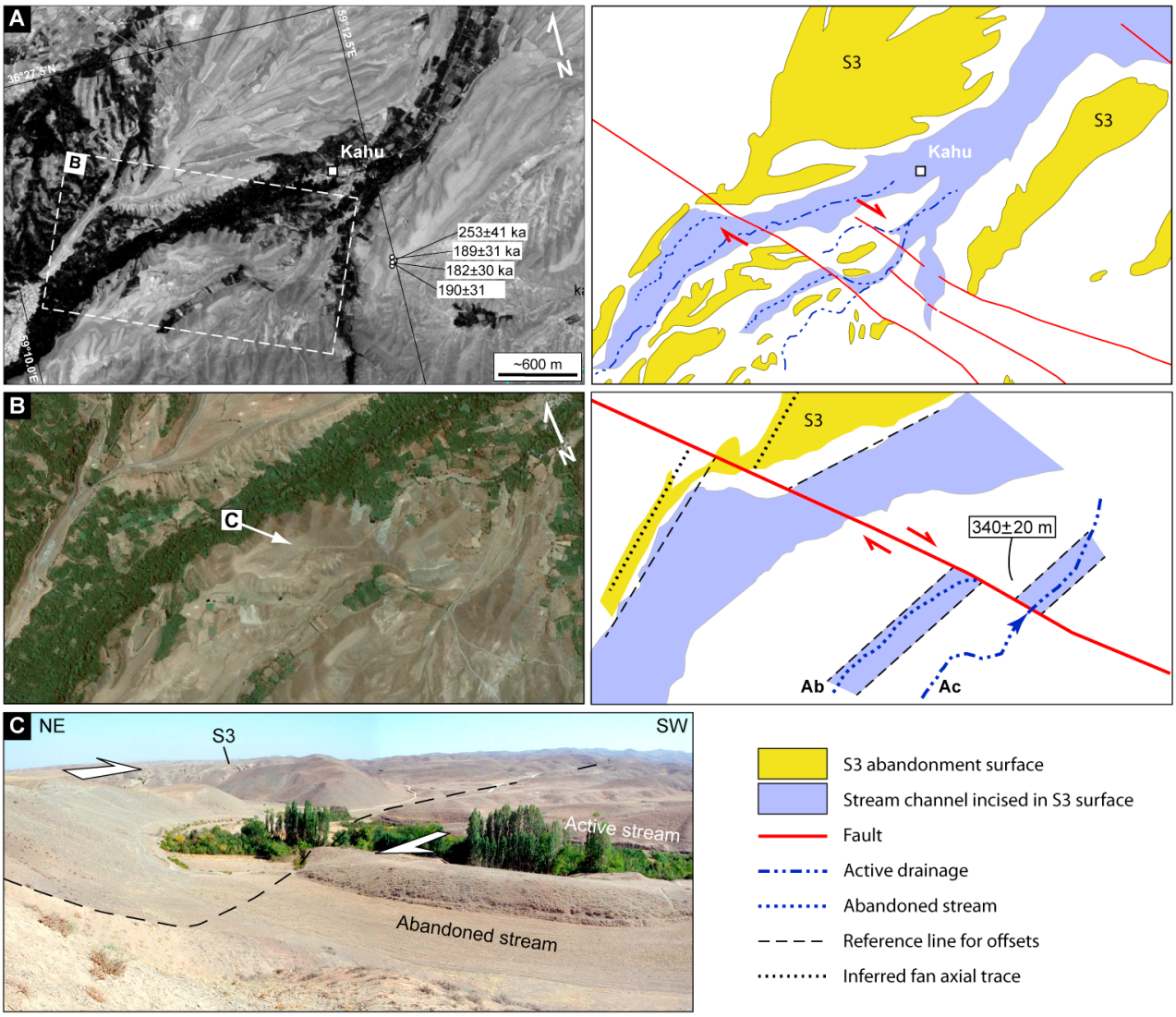

Figure 14. (a) SPOT-5 image and the morphotectonic map of the Kahu area, including the northwestern portion of the Mashhad Fault Zone. Sample locations and their exposure ages are shown (see Table 1 for sample information). (b) GeoEye image of the area in Figure 14a together with its morphotectonic interpretation (right). Piercing points are intersections of reference lines with the fault trace. Ab, Abandoned stream; Ac, Active stream. (c) Panoramic view of the stream abandoned due to dextral faulting along the fault. The location and look direction are marked in Figure 14b. Dashed line marks the trace of the Mashhad Fault.

phenakite [*Merchel et al.*, 2008]. Beryllium was separated from these solutions by successive solvent extractions and precipitations. Beryllium oxides were mixed with Niobium for target packing and samples were analyzed by Accelerator Mass Spectrometry (AMS). All ^{10}Be concentrations are normalized to ^{10}Be/^{9}Be SRM 4325 NIST reference material with an assigned value of $(2.79 \pm 0.03) \times 10^{-11}$. This standardization is equivalent to 07KNSTD within rounding error. The ^{10}Be half-life of $(1.39 \pm 0.01) \times 10^{6}$ years used is that recently recommended by *Korschinek et al.* [2010] and *Chmeleff et al.* [2010] according to their two independent measurements. Analytical uncertainties (reported as 1σ) include a conservative 0.5% external uncertainty based on long-term measurements of standards, a one-sigma statistical error on counted ^{10}Be events, and the uncertainty associated with the chemical blanks correction [*Arnold et al.*, 2010]. Two chemical blanks prepared with the samples yield similar ^{10}Be/^{9}Be ratio of 2.6×10^{-15} and 2.1×10^{-15}.

[33] To determine production rates, scaling factors for latitude and altitude corrections were calculated according to *Stone* [2000] and using a modern ^{10}Be production rate at sea level and high latitude of 4.5 ± 0.3 atoms/g SiO_2/yr to account for the reevaluation of absolute calibration of ^{10}Be AMS standards proposed by *Nishiizumi et al.* [2007]. The slow and fast muon contributions are from *Braucher et al.* [2011]. For all sampling sites, corrections for shielding by the surrounding topography, snow cover and sample

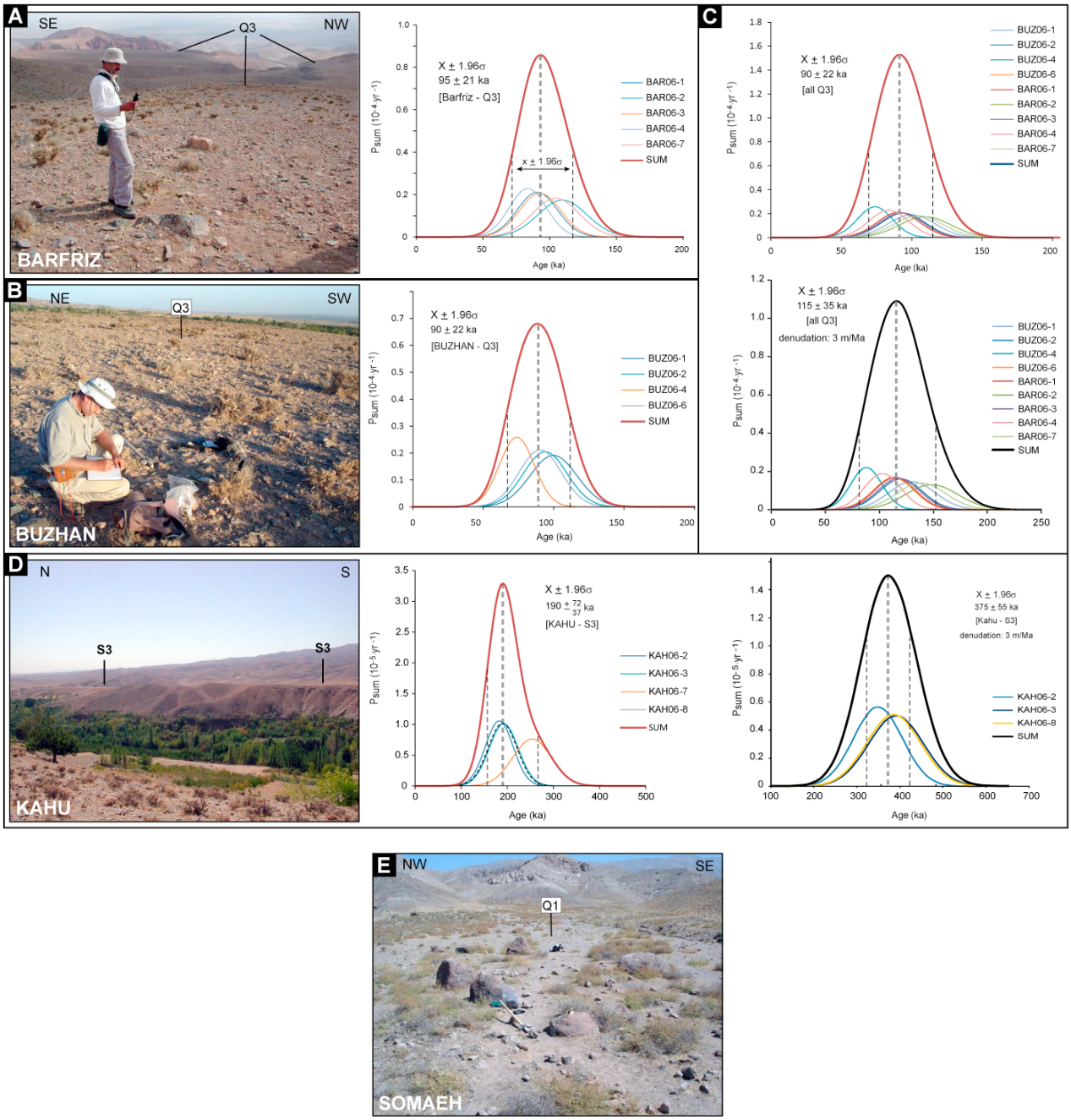

Figure 15. Field photographs illustrating general views of Q_1, Q_3, and S_3 alluvial abandonment surfaces together with Gaussian distributions of in situ-produced ^{10}Be exposure ages of surface samples. Thick curves are age probability sum, and thin curves represent the age probability for each individual sample (see section 6). (a and b) Shown are field photographs of Q_3 surfaces in the Barfriz (Figure 7) and Buzhan (Figure 5b) areas, respectively. Diagrams are the age distribution of related samples, assuming zero erosion. (c) Exposure age distribution of all samples from both the Barfriz and Buzhan Q_3 surfaces, with the assumptions of (top) zero erosion and (bottom) maximum erosion rate of 3 m/Myr. (d) S_3 surface in the Kahu area (field photograph) together with the age distribution of the surface samples; zero erosion (on the left) and maximum erosion rate of 3 m/Myr (on the right) hypotheses. (e) Q_1 surface in the apex of the Somaeh alluvial fan.

geometry, following *Dunne et al.* [1999], have negligible impact on the surface production rates.

[34] In this study, the determination of minimum exposure ages (Table 1) relies on the assumption that the effect of erosion on the most preserved part of the alluvial surfaces (i.e., sampled parts) is negligible. Two other sets of exposure ages (Table 1) were calculated using the maximum 3 m/Ma and suggested 1.8 mm/yr denudation rates (see section 6.3),

Table 1. Sample Characteristics and Exposure Ages[a]

Sample	Longitude (°E)	Latitude (°N)	Altitude (m)	Thickness (cm)	^{10}Be Production Rate (atoms/g SiO_2/yr)	^{10}Be (atoms/g SiO_2)	Age (ka)		
							Min	Max	Int
BAR06-1	58.9081	36.2926	1843	3	16.6701124	1477917 ± 60787	91 ± 15	114 ± 19	103 ± 17
BAR06-2	58.9079	36.2923	1839	4	16.62038235	1771386 ± 73503	109 ± 18	146 ± 24	128 ± 21
BAR06-3	58.9078	36.2923	1840	7	16.6345474	1506829 ± 62308	93 ± 15	117 ± 19	105 ± 17
BAR06-4	58.9075	36.2920	1841	5	16.64501092	1362434 ± 56382	84 ± 14	103 ± 17	94 ± 15
BAR06-7	58.9086	36.2957	1915	5	17.52567713	1784065 ± 72804	105 ± 17	137 ± 23	121 ± 20
BUZ06-1	58.9325	36.2345	1457	4	12.64092437	1230674 ± 50785	100 ± 16	129 ± 21	114 ± 19
BUZ06-2	58.9325	36.2345	1463	10	12.69732659	1165681 ± 41690	94 ± 15	119 ± 19	107 ± 17
BUZ06-4	58.9325	36.2345	1465	7	12.71428879	921267 ± 38630	74 ± 12	88 ± 14	81 ± 13
BUZ06-6	58.9325	36.2344	1462	7	12.68887315	1121215 ± 45581	90 ± 15	113 ± 19	102 ± 17
KAH06-2	59.2088	36.4352	1466	6	12.7909586	2229050 ± 73958	182 ± 30	349 ± 57	244 ± 40
KAH06-3	59.2089	36.4355	1463	5	12.76257517	2323869 ± 76485	190 ± 31	391 ± 63	261 ± 42
KAH06-7	59.2090	36.4353	1463	7	12.76252342	3038968 ± 99334	253 ± 41	—	253 ± 41
KAH06-8	59.2088	36.4352	1465	3	12.77956774	2314219 ± 77596	189 ± 31	385 ± 63	259 ± 42
SOM06-5	58.8583	36.2809	1390	6	12.0070892	64009 ± 8477	5.3 ± 1.1	5.4 ± 1.2	5.3 ± 1.1
SOM06-6	58.8583	36.2809	1390	7	12.0070892	27345 ± 7242	2.3 ± 0.5	2.3 ± 0.5	2.3 ± 0.5
SOM06-8	58.8582	36.2807	1389	8	11.99891658	51622 ± 11131	4.3 ± 1.2	4.3 ± 1.2	4.3 ± 1.2

[a]Note that ^{10}Be concentrations analytical uncertainties (reported as 1σ) include a conservative 0.5% external uncertainty based on long-term measurements of standards, a one sigma statistical error on counted ^{10}Be events, and the uncertainty associated with the chemical blanks correction [*Arnold et al.*, 2010]. Two chemical blanks prepared with the samples yield similar ^{10}Be/^{9}Be ratio of 2.6×10^{-15} and 2.1×10^{-15}. For CRE age calculations, a modern sea level high-latitude ^{10}Be production rate at of 4.5 ± 0.3 atoms/g/yr has been scaled for the sampling altitudes and latitudes using the scaling factors proposed by *Stone* [2000]. An additional 6% production rate uncertainty is considered for CRE age calculation [*Stone*, 2000]. Age min, minimum exposure ages assuming negligible erosion on the sampled fan surfaces; Age max, maximum exposure ages assuming a maximum denudation rate (3 m/Ma) reported for well preserved alluvial surfaces in north and central Iran [*Landgraf*, 2010; *Le Dortz et al.*, 2011]. For KAH06-7, the ^{10}Be concentration is saturated with a denudation rate of 2.8 m/Ma. Age int, the exposure ages interpreted as being close to the true age of the abandonment surfaces. A denudation rate of 1.8 m/Myr was used to calculate the ages. A density of 2.2 g/cm^3 has been used for the host alluviums to calculate the ages.

which allow us to evaluate possible variations in the exposure ages.

[35] To illustrate cosmogenic-derived minimum exposure age data and their associated uncertainties, we used the sum of the Gaussian probability distributions [e.g., *Deino and Potts*, 1992], already used by different authors for dating purposes [e.g., *Lowell*, 1995], according to [e.g., *Taylor*, 1997]

$$p_{sum}(t) = \sum_i e^{-(t-a_i)^2/2\sigma_i^2}/\sigma_i\sqrt{2\pi} \quad (1)$$

where t is time, a_i is the exposure age of sample i and σ_i is the associated uncertainty. The probability of 68%, i.e., 1σ, was chosen to calculate uncertainties associated with surface exposure ages:

$$\sigma^2 = \frac{1}{(N-1)}\sum_{i=1}^{i=N}(t_i - \bar{t})^2 \quad (2)$$

6.1. Exposure Ages of Alluvial Fans Offset by the Neyshabur Fault System

[36] To verify the simultaneous abandonment of Q_3 surfaces throughout the foothills domain, two Q_3 fan surfaces were sampled at two different localities. Five samples were collected from quartz-rich sandstone boulders embedded in the well-preserved Barfriz alluvial fan surface (Figures 7b and 15a). Four quartz cobbles were sampled from another Q_3 fan surface that is of the rare well preserved Q_3 surfaces in the hanging wall of the Eyshabad Fault (Figure 15b).

[37] For the Barfriz abandonment surface, the five samples collected from two most well-preserved parts of the Q_3 surface (Figure 7b) yield minimum exposure ages ranging between 84 ± 14 and 110 ± 18 ka, with a weighted mean exposure age of 95 ± 11 ka (Figure 15a and Table 1). The sum of the Gaussian age probability distributions (P_{sum}) shows a sharp peak at 95 ka, with no outliers (Figure 15a).

[38] The four samples, from the other fan surface, yield minimum ^{10}Be exposure ages between 74 ± 12 and 100 ± 16 ka. The weighted mean value of these ages is 90 ± 11 ka (Figure 15b and Table 1), close to the weighted mean age of 95 ± 21 ka for the Barfriz surface. Except for one sample, which is slightly younger (74 ± 12 ka), 8 of the 9 samples from the two Q_3 surfaces yield exposure ages between 84 ± 14 and 110 ± 18 ka, with a weighted mean age of 90 ± 11 ka (Figure 15c). The consistent ages of all samples from both Q_3 fan surfaces strengthen our confidence for the isochronous abandonment of Q_3 surfaces spread throughout the foothills domain, whatever their geomorphic and structural settings (Figures 15a–15c).

[39] In summary, the minimum age of the Q_3 abandonment surface is statistically constrained by eight sample ages that cluster tightly around a weighted mean age of 90 ± 11 ka assuming that there has been no significant erosion to affect in situ-produced cosmogenic ^{10}Be concentrations in the samples (see section 6.3).

[40] Along the Somaeh fault, only 3 of 10 andesitic samples collected from boulders embedded in the offset Q_1 alluvial fan surface (Figures 9b and 15e) provided minimum pure quartz masses necessary for the analytical procedure of ^{10}Be dating. The three analyzed samples yield minimum exposure ages of 2.3 ± 0.5, 4.3 ± 1.2 and 5.3 ± 1.1 ka (Table 1). The insufficient sample ages do not lead to a reliable mean age representative of the fan abandonment. However, Q_1 fan surfaces are well preserved and it is unlikely that boulders currently at the surface were exposed by denudation. In such a case, the boulder exposure ages might be dispersed due to heterogeneous decrease in

Table 2. Maximum Denudation Rates (Steady State) for the Kahu Abandonment Surface (S_3)[a]

Sample	Shielding Factor	Production Rate (Muons) (atoms/g/yr)	Internal Uncertainty (m/Ma)	Erosion Rate (g/cm^2/yr)	Erosion Rate (m/Myr)	External Uncertainty (m/Myr)	Production Rate (Spallation) (atoms/g/yr)
KAH06-2	0.99	0.289	0.07	0.00089	4.04	0.36	12.52
KAH06-3	0.99	0.289	0.06	0.00085	3.87	0.35	12.49
KAH06-7	0.99	0.288	0.04	0.00061	2.79	0.26	12.49
KAH06-8	0.99	0.291	0.08	0.00087	3.95	0.36	12.51

[a]Scaling schemes for spallation are from *Lal* [1991] and *Stone* [2000]. The rates were calculated using the CRONUS-Earth online calculator (http://hess.ess.washington.edu/math/).

concentration of ^{10}Be cosmogenic nuclides in boulders according to their mineralogical compositions. In both cases, the actual age of the fan abandonment surface might be close to the 4.2 ± 1.2 and 5.2 ± 1.1 ka older ages, with a mean age of 4.8 ± 1.7 ka.

6.2. Exposure Ages of Alluvial Fans Offset by the Mashhad Fault Zone

[41] From S_3 surfaces, we dated a total of four samples of quartz boulders (Figure 15d and Table 1) embedded in the most preserved part of a fan surface extended downhill from the fault (Figure 14a). Three of four samples yield minimum ^{10}Be exposure ages of 182 ± 30, 190 ± 31 191 ± 31, but one sample is significantly older (254 ± 42 ka). For all samples, the sum of the Gaussian age probability distributions (P_{sum}) shows a single peak with no outlier (Figure 15d). A weighted mean ^{10}Be exposure age of 190 ± 37 ka, thus, represents the "minimum possible" age for the S_3 abandonment surface.

6.3. Effects of Erosion and Surface Denudation on ^{10}Be Exposure Ages

[42] Erosion minimizes exposure ages of samples collected from top of abandonment surfaces by decreasing cosmogenic isotope concentrations. In a lack of direct erosional features, even young gullies and significant differential erosion on the sampled parts of the alluvial fan surfaces (Figure 15), one may attribute the current position of large clasts collected from the fan surfaces to erosion processes which cause upward migration of clasts to the land surfaces [e.g., *Thomas*, 1989; *Cooke et al.*, 1993; *Wells et al.*, 1995]. In such cases, clasts are concentrated at the land surface at significantly different times, and thus, a random surface sampling will show considerable scatter in the ages of clasts [e.g., *Bierman*, 1994; *Zreda et al.*, 1994; *Phillips et al.*, 1997]. In contrast, *Phillips et al.* [1997] and *Zreda et al.* [1994] showed that for the surfaces undergoing small denudation depths, apparent ages are clustered together and their mean age is the best estimate (±10%) of the true landform age, even determined with only a few samples from the surface [see also *Bierman*, 1994]. It is worth noting that the erosion rate affecting surface boulders may be significantly lower than the denudation rate estimated for the corresponding surfaces [e.g., *Ritz et al.*, 2006a].

[43] The fact that the exposure ages, especially for Q_3 surfaces, are coherent and well clustered (Figure 15) may indicate that the clasts have stayed at the fan surfaces regardless of erosion processes (if any). Such a suggestion is likely to be valid; available postabandonment denudation rates for well-preserved alluvial surfaces, in the Iranian plateau, are low [*Regard et al.*, 2006; *Authemayou et al.*, 2009; *Le Dortz et al.*, 2011]. In central Iran, *Le Dortz et al.* [2011] reported a low denudation rate of 1 m/Ma by analyzing cosmogenic ^{10}Be and ^{36}Cl in surface cobbles and near surface amalgams collected from alluvial terraces (abandoned between 10 and 300 ka). Using both surface and depth profile samples from alluvial fans, *Authemayou et al.* [2009] concluded that the abandonment surfaces, in the Zagros Mountains, have remained stable during the last ~170 ka. However, this rate could be higher in wetter regions involved in compressional tectonic regimes; for instance, at the southern flank of central Alborz, the rate of surface denudation ranges from ~0.3 to ~3.0 m/Ma for well-preserved alluvial terraces [see *Landgraf*, 2010]. These imply denudation rates varying between "negligible" and 3 m/Ma for nearly pristine alluvial abandonment surfaces, according to both climate conditions (dry/wetter) and tectonic regimes (strike-slip/compressional). As expected, the Mediterranean xeric continental climate condition in the Binalud region [e.g., *Djamali et al.*, 2011] implies a climate regime less humid than south central Alborz, and less arid than central Iran climate regimes. Interestingly, for the oldest surface (S3), the maximum denudation rate (steady state) is estimated between 2.8 and 4 m/Ma; higher denudation rates would lead to nuclide concentrations lower than that we measured in the surface samples (Table 2).

[44] Despite our special care during sampling to minimize the effects of erosion, the negligible erosion hypothesis leads our exposure ages, except for the Q_1 surface, to the minimum age for the alluvial fan abandonment surfaces. Therefore, we calculated two other sets of ^{10}Be ages (Table 1 and Figures 15c and 15d) using mean and maximum denudation rates of 1.8 and 3 m/Ma, respectively. The three sets of exposure ages in Table 1 allow us to evaluate maximum possible variations in the ages and consequently in our estimates of fault slip rates. Applying the 1.8 m/Ma denudation rate on the Kahu surface (S_3), the three "apparently younger" samples yield exposure ages similar to the oldest age of ~250 ka (Kah06-7; "Age min." in Table 1) calculated using zero erosion. Accordingly, we have used the denudation rate of 1.8 m/Ma to recalculate exposure ages, which we suggest are close to the true ages for the Q_3 and S_3 abandonment surfaces. That is, the mean ages of 105 ± 14 ka, and 255 ± 15 ka for the Q_3 and S_3 abandonment surfaces, respectively. Further work incorporating depth profiles and other appropriate Quaternary dating methods will better constrains denudation rates and true ages of the alluvial fan abandonment surfaces.

7. Fault Slip Rates

[45] Our slip rate estimates are based on two main assumptions: (1) the fault slip rates remained constant since the initiation of cumulative fault offsets and (2) the main

Table 3. Possible Variations in Slip Rates According to the Minimum and Maximum Exposure Ages for Binalud Mountain Range[a]

Fault Name			Displacement (m)		^{10}Be Exposure Age (ka)		Slip Rate (mm/yr)	
System	Zone	Fault	Type	Value	Minimum	Maximum	Minimum	Maximum
Neyshabur	Barfriz		V	140 ± 50			1.2 ± 0.5	1.6 ± 0.6
			H	240 ± 20			2.1 ± 0.4	2.7 ± 0.4
			O	280 ± 100			2.4 ± 1.0	3.1 ± 1.2
	Buzhan	Eyshabad	V	85 ± 30	90 ± 11	115 ± 18	0.7 ± 0.3	0.9 ± 0.4
		Somaeh	V1	∼60			∼0.5	∼0.7
			V2	2.1 ± 0.1	4.7 ± 1.7	4.8 ± 1.7	0.4 ± 0.2	0.4 ± 0.2
		Qadamgah	H	260 ± 40			2.3 ± 0.5	2.9 ± 0.6
	Buzhan		V	145 ± 35			1.3 ± 0.4	1.6 ± 0.4
Neyshabur			V	290 ± 50	90 ± 11	115 ± 18	2.5 ± 0.6	3.2 ± 0.7
			H	250 ± 45			2.2 ± 0.5	2.8 ± 0.6
			O	380 ± 95			3.3 ± 1.0	4.3 ± 1.2
	Mashhad		H	340 ± 20	190 ± 37	375 ± 45	0.9 ± 0.1	1.8 ± 0.4

Parameters	Criteria	Slip Rate (mm/yr)	
		Minimum	Maximum
Shortening[b]	Constant fault geometry with depth	1.5 ± 0.4	1.9 ± 0.5
	If thrusts flatten with depth	2.0 ± 0.7	2.5 ± 0.8
Horizontal	central Iran–East Kopeh Dagh	3.4 ± 1.2	4.9 ± 1.7
Uplift	SE part of Binalud	2.5 ± 0.6	3.2 ± 0.7
Northward	central Iran–East Kopeh Dagh	∼3.2	∼4.5

[a]Type of offset: V, vertical; H, horizontal; O, oblique calculated using H and V.
[b]See the section 8.2 for more details. For uncertainties of the displacements refer to related geomorphic reconstructions. Minimum and maximum slip rates are based on the maximum and minimum ages suggested for the abandonment surfaces (see Table 1 for more information).

fault strands have taken up nearly all the deformation. If accepted, the accuracy of our slip rates depends on the accuracy of ^{10}Be exposure ages, and their geomorphic relevance to the cumulative fault offsets. It is worth noting that the slip rates discussed in this section are based on the ^{10}Be exposure ages calculated using a denudation rate of 1.8 m/Ma for the abandonment surfaces. The minimum and maximum slip rates deduced from the maximum (denudation rate of 3 m/Ma) and minimum (zero erosion assumption) ^{10}Be ages, respectively, are listed in Table 3 in order to illustrate the possible variations in the fault slip rates.

[46] Along the southwest piedmont of the Binalud Mountains, Q_3 alluvial fan surfaces form a key regional geomorphic marker that allowed us to characterize the Quaternary deformation due to the Neyshabur Fault System. We concluded that Q_3 fan surfaces were simultaneously abandoned at 105 ± 14 ka, as indicated above. Along the Barfriz Fault, Q_3 surfaces have recorded the cumulative oblique displacement of 280 ± 100 m, which corresponds to a reverse vertical component of 140 ± 50 m combined with a right-lateral component of 240 ± 20 m. These offset values yield a Quaternary slip rate of 2.6 ± 1.0 mm/yr for the oblique faulting. This corresponds to vertical and horizontal slip rates along the Barfriz Fault of 1.3 ± 0.5 and 2.3 ± 0.4 mm/yr, respectively.

[47] Along the Buzhan Fault Zone, the reconstruction of depositional geomorphology of Q_3 surfaces (Figures 8a and 8b) reveals a cumulative vertical offset of 145 ± 35 m yielding the slip rate of 1.4 ± 0.4 mm/yr averaged over a time period of ∼105 ka. For the Qadamgah Fault, a slip rate of 2.5 ± 0.5 mm/yr is estimated for its strike-slip component of motion applying the age of Q_3 abandonment surface (105 ± 14 ka) to the cumulative offset of 260 ± 40 m expressed by streams incised in Q_3 surfaces.

[48] At the southwestern extension of the Neyshabur Fault System, Q_1 alluvial fans provide evidence of Holocene faulting; their abandonment is suggested at 4.8 ± 1.7 ka. In the Somaeh area, a Q_1 alluvial fan has recorded a sum of 2.0 ± 0.1 m of vertical displacement expressed in two distinct fault offsets: (1) a cumulative vertical offset of 1.4 ± 0.2 m along the main trace of the Somaeh Fault and (2) a vertical offset of ∼0.80 m along a younger fault segment southeast of the main trace of the fault (Figures 9d and 11b). These yield the Holocene slip rate of 0.4 ± 0.2 mm/yr for vertical displacement on the Somaeh Fault (Figures 10 and 11). This rate is in the same order than the slip rate of ∼0.6 mm/yr deduced from the cumulative vertical offset of ∼60 m which is recorded by Q_3 surfaces during the last 105 ± 14 ka. Nevertheless, given the short time period of ∼5 ka, the Holocene slip rate averages the actual slip rate of the fault because it is unclear when the oldest rupture-associated earthquake occurred relative to the age of the displaced fan [see *Berberian and Yeats*, 1999].

[49] Along the northwestern part of the Mashhad Fault Zone, the Kahu alluvial surface (S_3) has recorded a right-lateral cumulative offset of 340 ± 20 m (Figure 14b), suggesting the abandonment of S_3 surface at 255 ± 15 ka, a Late Quaternary slip rate of 1.3 ± 0.1 mm/yr is calculated. Given a lack of significant vertical displacements observed along the fault, and given the nearly vertical geometry of the fault zone, the lateral slip rate of 1.3 ± 0.1 mm/yr is considered here as representative of the overall motion of the Binalud Mountains relative to their eastern side, parallel to the Mashhad Fault Zone (N320°E).

8. Discussion

8.1. Deformation Pattern of the Binalud Mountains

[50] Like other fold-and-thrust belts, e.g., Taiwan [*Davis et al.*, 1983], India and Pakistan [*Yeats*, 1986], the Transverse Ranges [*Namson and Davis*, 1988; *Bullard and Lettis*, 1993] and the San Joaquin Valley of California [*Keller et al.*, 2000],

the topographic expression of the Binalud Mountains has been mostly produced by the ongoing thrust faulting and folding [e.g., *Alavi*, 1992]. In active fold-and-thrust belts, the deformation commonly migrates away from the highlands of the range toward the adjacent flanks. Interior faults of the system may become relatively inactive as the active tectonic processes are transferred to frontal fault systems [e.g., *Davis et al.*, 1983; *Yeats*, 1986, and references therein]. In the same way, but at a smaller scale, the topography and regional geomorphology of the Binalud Mountains are closely associated with geometry, kinematics and distribution of active faulting along the bounding faults (i.e., the Neyshabur Fault System and the Mashhad Fault Zone).

[51] In addition to these common modes of deformation known from the typical fold-and-thrust belts, the structural and geomorphic evolution of the Binalud Mountains are influenced by the right-lateral shear between central Iran and Eurasia. In its southeastern half, the Binalud appears to be an asymmetric mountain range characterized by a short and steeply sloping southwest flank versus a long and gently sloping northeast flank which is occupied by elongated and more linear drainage basins. This geometry can be explained by differing faulting mechanisms for the Neyshabur Fault System and the Mashhad Fault Zone (Figure 2a) producing differential vertical movements on both sides of the range. The southwest flank is uplifted due to reverse faulting along the Neyshabur Fault System, while the northeast flank is affected by strike-slip faulting along the Mashhad Fault Zone. Interestingly, these geomorphic and geometric characteristics are only observed within the southeastern half of the range where the Binalud Mountains are restrained between the overlapping range-bounding faults (Figure 16).

[52] The Binalud Mountains are deformed between the oblique-slip Neyshabur Fault System and the strike-slip Mashhad Fault Zone bounding the southwest and northeast sides of the range, respectively. Moreover, at the northwestern range border, the strike-slip Chakaneh Fault System (Figures 2a and 16) plays an important role transferring a part (≥2 mm/yr) of active strike-slip faulting between the Kopeh Dagh Mountains and the Neyshabur Fault System [*Shabanian et al.*, 2009b]. On the northeast side of the range, the Mashhad Fault Zone slips right-laterally (1.3 ± 0.1 mm/yr) without direct structural connection to the Kopeh Dagh fault systems (Figure 2a). The right-handed arrangement of the Neyshabur Fault System and the Mashhad Fault Zone, which are characterized by the respective oblique-slip reverse and strike-slip fault kinematics, forms a soft-linked restraining step over. This can be regarded as a dextral relay zone in which the deforming southeastern half of the Binalud Mountains forms a crustal-scale pop-up structure (Figure 16). In this context, shortening (1.6–2.2 mm/yr) and uplift (~2.8 mm/yr) is taken up by reverse component of faulting on the Neyshabur Fault System.

[53] Interestingly, the along-strike differences in the structural pattern have been recorded in the long-term geomorphic evolution of the range. The deeply incised topography of the southeastern half contrasts with the pristine geomorphology of the northwestern half in which the elevated remnant of a Mesozoic paleorelief exhibits its former erosional surface as a flat summit plateau (Figures 2a and 16). As it is characterized by remnants of upper Mesozoic rocks cropping out in several places (Figure 2a), we suggest that the Lower Triassic metamorphic core of the Binalud was initially covered by Upper Mesozoic marine carbonates. During Cenozoic, these rocks were totally removed from the southeastern half. The most preserved parts of the Mesozoic paleorelief is found far from the restraining relay zone, where the paleorelief is bounded by the strike-slip Chakaneh Fault System. The variation in the topography and geomorphology of the range implies a close relationship between denudation and long-term tectonic movements controlled by along-strike variations in the structural pattern of the range. The incised, high topography of the southeast Binalud Mountains resulted from shortening and the related uplifting within the restraining relay zone between the Neyshabur Fault System and the Mashhad Fault Zone (Figure 16). In contrast, there is no evidence of significant vertical movement in the northern half of the range affected by the pure strike-slip Chakaneh Fault System (Figures 2a and 16).

[54] Another possible explanation for this along-strike geomorphic difference is that the Mashhad Fault Zone is propagating to the northwest, and so has not yet disrupted the erosion surface (Mesozoic paleorelief) farther northwest. This seems consistent with the fact that deformation is localized on a single strand to the southeast on a more mature fault zone, and is distributed on various less mature strands to the northwest. However, we lack adequate data to choose between these two possibilities, which are not mutually exclusive and may, in fact work together. Further data will better constrain the situation and favor one (or more) possibilities over others.

[55] At the scale of the Binalud restraining zone, the basinward migration of the depositional zones of Q_3, Q_2, and Q_1 alluvial fans indicate the migration of deformation locus away from the highlands of the range such that the youngest structures are at the edge of the range. During the deposition of Q_3 alluvial fans, the front of the Binalud Mountains corresponded to the Barfriz Fault. As the mountain front developed, new faults formed basinward and a new mountain front has developed. Older alluvial fans were tilted, faulted, and incorporated within the foothills domain (Figures 3, 4b, and 5c). The older, now intermountain front, i.e., the Barfriz Fault Zone, has been abandoned in the interior of the range, and new fans were developed basinward. Late Holocene fault activities (≤5 ka) are expressed in vertical fault offsets recorded by Q_1 alluvial fans which were formed downhill from the southwestern extension (external limit) of the Buzhan Fault Zone (e.g., the Somaeh Fault). The youngest fault activity is represented by basinward development of fault ruptures (Figure 9) or up-warped alluvial fans indicating the active front of deformation ~4.8 km southwest of the older mountain front (Barfriz Fault Zone). These observations clearly reveal the basinward migration of deformation locus and the across-range growth of the Binalud Mountains during the last ~100 ka.

8.2. Implications for the Geodynamics of Northeast Iran

[56] As for the Neyshabur Fault System, we estimated a horizontal slip rate of 2.4 ± 0.5 mm/yr which is an average of slip rates determined from the cumulative offsets measured on the Qadamgah Fault and the Barfriz Fault Zone. The total 290 ± 50 m vertical deformation deduced from the geomorphic reconstruction of Q_3 fan surfaces (Figures 8a and 8b) yields an uplift rate of 2.8 ± 0.6 mm/yr averaged over 105 ± 14 ka. If the fault geometry of N135°E/60 ±

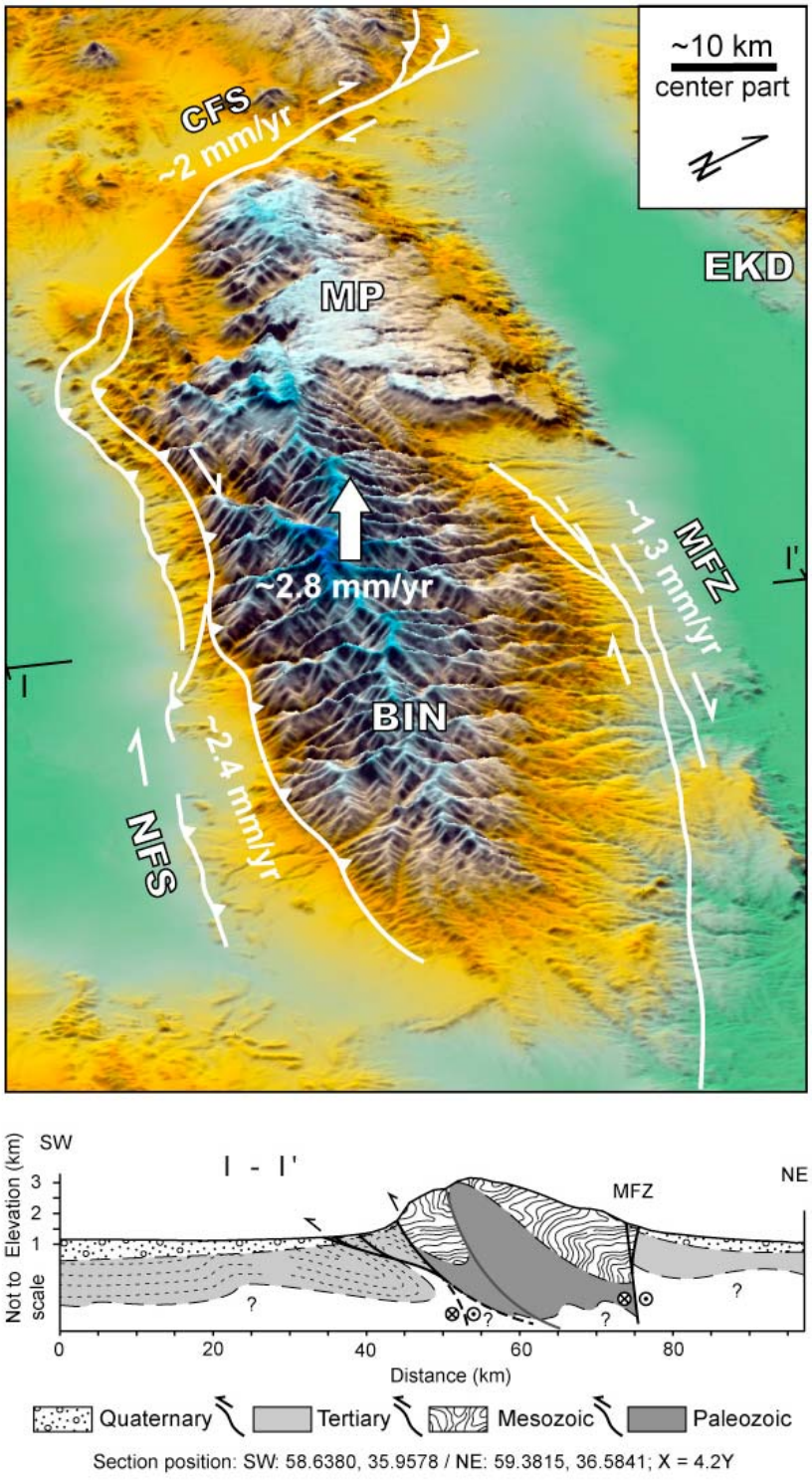

Figure 16. (top) A 3-D view of the Binalud Mountains based on SRTM topographic data representing general morphology of the mountains, major fault systems (thick white lines), as well as the vertical and horizontal slip rate estimates on both sides of the range. Slip rate for the Chakaneh Fault System (CFS) was taken from *Shabanian et al.* [2009b]. BIN, Binalud; MFZ, Mashhad Fault Zone; NFS, Neyshabur Fault System; MP, Mesozoic Plateau; EKD, eastern Kopeh Dagh; Eu, Eurasia. (bottom) Schematic cross section of the Binalud Mountains illustrating the inferred structure and the migration of the locus of active faulting within the Binalud restraining relay zone. Gray line marks inactive faults. The topographic profile is based on SRTM data.

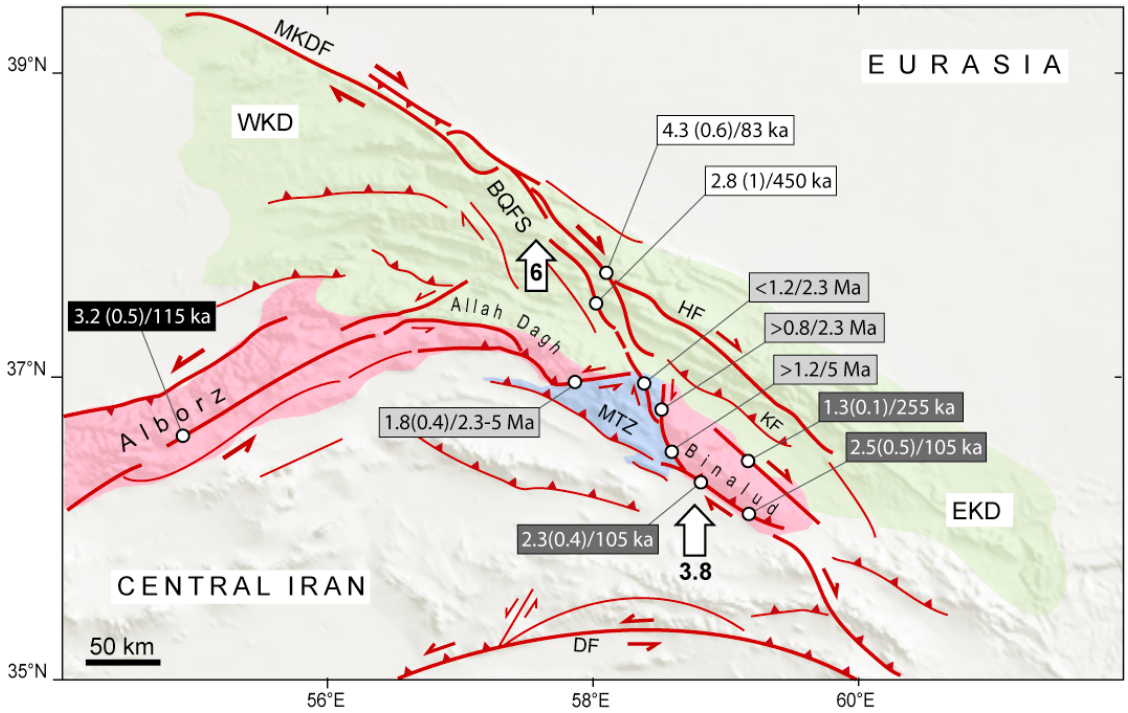

Figure 17. Regional integration of geological fault slip rates in northeast Iran. Slip rates and associated uncertainties (within parentheses) are followed by the time over which the rates were estimated. White boxes from *Shabanian et al.* [2009a] (^{36}Cl ages); light gray boxes from *Shabanian et al.* [2009b] (Ar-Ar ages); dark gray boxes from this study (^{10}Be ages); the black box from *Javidfakhr et al.* [2011b] (^{10}Be age). White arrows are the geologically derived northward motion (in mm/yr) of central Iran relative to eastern Kopeh Dagh. Abbreviations: MKDF, Main Kopeh Dagh Fault; BQFS, Bakharden-Quchan Fault System; DF, Doruneh Fault; MTZ, Meshkan Transfer Zone; KF, Kashafrud Fault; HF, Hazarmasjed Fault; EKD, eastern Kopeh Dagh; WKD, western Kopeh Dagh.

5°NE (Figures 7c, 9e, and 12b) remains constant with depth, this uplift is accounted by a 1.6 ± 0.4 mm/yr shortening rate perpendicular to the Binalud Mountains. But, if the thrusts in the Buzhan Fault Zone flatten with depth then the horizontal convergence rate would be higher than this value (see *Hollingsworth et al.* [2010] for more information). In this case, the shortening rate across the Neyshabur Fault System will be the sum of vertical slip rates (1.4 ± 0.4 mm/yr) of the Buzhan Fault Zone and the shortening rate (0.8 ± 0.3 mm/yr) across the Barfriz Fault, i.e., 2.2 ± 0.7 mm/yr. As indicated by *Hollingsworth et al.* [2010], the geometry of geological structures across the fault system allows the differentiation between these two models, and to determine the correct shortening rate estimate. Actually, given the asymmetric SW verging fold geometry between the Barfriz and Buzhan Fault Zones (Figure 5c), it is not very likely that the Buzhan Fault Zone flattens at shallower depth above a horizontal décollement. However, the fault dips may change with depth (do not confuse with flattened faults). In such a case, we incorporate both shortening rate estimates as upper and lower bounds, yielding 1.6–2.2 mm/yr. These rate estimates are, of course, higher than the shortening rate (0.3–1.0 mm/yr) proposed by *Hollingsworth et al.* [2010], who only considered the Eyshabad Fault.

[57] The range-parallel right-lateral (2.4 ± 0.5 mm/yr) and range-perpendicular shortening rates (1.6–2.2 mm/yr) allowed us to estimate the horizontal motion of central Iran relative to the Binalud Mountains at a late Quaternary rate of 2.9 ± 1.0 mm/yr in the N350 ± 13°E direction. In the same way, the addition of the 1.3 ± 0.1 mm/y lateral slip rate on the strike-slip Mashhad Fault Zone yields the overall motion of central Iran relative to eastern Kopeh Dagh at a rate of 4.0 ± 1.3 mm/yr, in N340 ± 8°E direction.

[58] The regional integration of the slip rates gives a coherent image of the deformation field in northeast Iran (Figure 17). As suggested by *Shabanian et al.* [2009a], almost 80% (~6 mm/yr) of the total ~8 mm/yr of the central Iran–Eurasia northward motion is localized along the Bakharden-Quchan Fault System in Kopeh Dagh (Figure 17). Our slip rate estimates indicate that the Binalud Mountains take up ~3.8 mm/yr (~60%) of this northward motion through dextral oblique-slip to strike-slip faulting localized on the SW and NE sides, respectively. It is likely that the remaining part (~40%) of the overall deformation is distributed on other dextral and reverse faults in eastern Kopeh Dagh such as the Hazarmasjed and Kashafrud Faults (Figure 17).

8.3. Integrating Data-Derived Results Within Preexisting Tectonic Models

[59] The range parallel oblique-slip to strike-slip faulting on both sides of the Binalud Mountains shows that the northward motion of central Iran relative to Eurasia has not wholly been absorbed by crustal shortening and thrust faulting in the range [e.g., *Berberian and Yeats*, 1999;

Hollingsworth et al., 2010]. This knowledge adds another piece to the geodynamic puzzle of northeast Iran (1) indicating the significant contribution of the Binalud faults to the accommodation of active deformation in northeast Iran and (2) suggesting that the Mashhad and Neyshabur Faults (bounding the Binalud Mountains) define the continuation of the northeastern Arabia-Eurasia intraplate boundary beyond Kopeh Dagh [e.g., *Shabanian et al.*, 2009a]. This also strengthens the suggestion that the Miocene–early Pliocene shortening and crustal thickening, at the scale of northeast Iran, were dominated by the present-day oblique-slip to strike-slip faulting localized along well-defined fault systems [*Shabanian et al.*, 2009b].

[60] The kinematics of active deformation in northeast Iran has been a matter of debate [see *Shabanian et al.*, 2009b, and references therein; *Siame et al.*, 2009]. The last kinematic model has been proposed by *Hollingsworth et al.* [2010] describing the geometry and kinematics of northeast Iran by oroclinal folding. The Binalud Mountains forms the eastern limb of the oroclinal fold, with small contribution (minor thrust faulting) to accommodate active deformation [*Hollingsworth et al.*, 2010]. This model is based on the simple assumption that the Alborz Mountains, with a complex Cenozoic tectonic history [e.g., *Stöcklin*, 1974; *Berberian and King*, 1981; *Alavi*, 1992; *Axen et al.*, 2001; *Ritz et al.*, 2006b; *Zanchi et al.*, 2006, *Guest et al.*, 2007; *Shabanian et al.*, 2009b; *Ballato et al.*, 2011; *Javidfakhr et al.*, 2011a; *Sheikholeslami and Kouhpeyma*, 2012], were initially a uniform E-W mountain range. Interestingly, this model requires that the geometry and kinematics of the east and west oroclinal limbs (i.e., deformation zone boundaries) evolve with time as the oroclinal folding develops. Such significant variations in the geometry of the Alborz and Kopeh Dagh deformation zones directly discard the main assumption (constant zone boundaries) of the previous model [*Hollingsworth et al.*, 2006] on which the present model is built. Consequently, this annuls both model-derived slip rates and ages estimated by the authors. Additionally, a simple but fundamental problem with this model is that folding at the scale of the Alborz Mountains (oroclinal) due to the northward motion of central Iran–Eurasia requires an "indenter", as is the case of the Talesh–western Alborz mountains indented by the South Caspian rigid block [see *Berberian*, 1983; *Djamour et al.*, 2010; *Shabanian et al.*, 2012]. In other words, the South Caspian Basin persists against the northward motion of central Iran, deforming the western portion of the Alborz range from an "assumed" E-W orientation. But, it is very unlikely that the deforming continental domain between the ~E-W Doruneh Fault, as the southern boundary for the northeast Iranian deformation domains, and the Allah Dagh–Binalud Mountains behaves as an indenter, folding the mountains. A nearly similar tectonic model was proposed by *Walker and Jackson* [2004] to explain the ~70 km northward curvature of the Doruneh Fault due to the northward motion of central Iran and Lut block relative to Eurasia. The structural and geomorphic studies carried out by *Farbod et al.* [2011] reveal that neither kinematics nor geometry of the Doruneh Fault can be described by such a structural model.

[61] Given the diachronous formation to closure of the eastern and western Kopeh Dagh basins [*Afshar Harb*, 1979; *Lyberis and Manby*, 1999] and the lack of thrust faulting along the Mashhad Fault Zone since the Devonian time [*Majidi*, 1978], we suggest that the overall shape of the Kopeh Dagh and Binalud mountains has principally been controlled by the former geometry of the north (Eurasia) and south (central Iran) margins. That is, the mountain belt never had an E-W linear orientation. The homogeneity, at the scale of northeast Iran, of the Miocene-Pliocene and Quaternary stress states [*Shabanian et al.*, 2010, 2012; *Javidfakhr et al.*, 2011a] argues for the fact that no significant change has occurred in the orientation of the belt since at least the Miocene. Otherwise, the stress state should significantly change in either limb, and in the hinge area of the "inferred" oroclinal. Afterward (3–5 Ma), the geometry of the belt has been slightly changed and adjusted accommodating strike-slip faulting oblique to the Alborz and Kopeh Dagh mountain ranges [*Shabanian et al.*, 2009a, 2009b; this study]. In the active tectonic context, reverse faulting is localized along the WNW trending faults [e.g., *Shabanian et al.*, 2010] that take up the reminders of deformation not transferred by strike-slip faulting. The fact that the Binalud mountains is deformed as a soft-linked restraining relay zone (section 8.1) favors the northward translation of central Iran with respect to Eurasia.

9. Conclusion

[62] In this paper, we provided new geomorphic and geological constrains on active faulting on both sides of the Binalud Mountains. Three regional episodes of alluvial surface abandonment were dated at ~4.8 ka (Q_1), ~105 ka (Q_3), and ~255 ka (S_3). Cumulative offsets recorded by Q_3 fan surfaces yield an oblique slip rate of 3.6 ± 1.0 mm/yr for right-lateral reverse faulting along the Neyshabur Fault System. For the Mashhad Fault Zone, the reconstruction of the cumulative right-lateral offset recorded by S_3 surfaces yields a Quaternary slip rate of 1.3 ± 0.1 mm/yr. The total slip rate of ~4.0 mm/yr across the Binalud Mountains implies the northward motion of central Iran relative to eastern Kopeh Dagh at a rate of ~3.8 mm/yr.

[63] The geometry, kinematics and arrangement of the range-bounding faults have controlled the long-term deformation and denudation history of the Binalud Mountains. Deformation patterns of the southeastern half of the range can be described by a soft-linked restraining step over in a largely dextral system. In such a system, the maximum uplift is predicted to occur within the region of fault overlap, and can explain the nonuniform pattern of deformation along the strike of the range.

[64] New structural and geomorphic constrains, such as detailed fault mapping, Quaternary offsets and slip rates, on active faulting of the Binalud Mountains argue for the localized faulting model, instead distributed deformation, in northeast Iran. Nevertheless, further detailed tectonic geomorphology investigations on active faults in eastern Kopeh Dagh will shed more light on the kinematics of active deformation at the northeastern boundary of the Arabia-Eurasia collision zone.

[65] **Acknowledgments.** This work was funded by the INSU-CNRS (France) and the International Institute of Earthquake Engineering and Seismology (IIEES, Iran), supervised by D. Hatzfeld and M. Ghafouri Ashtiani. Funding was provided by the Dyeti and PNRN programs (INSU-CNRS), and ACI FNS program (French Ministry of Research). SPOT images were provided thanks to the ISIS program (©CNES 2004 to 2007, distribution SPOT images S.A.). We thank V. Grimault, C. Duhamel and the staff of the SCAC of the French Embassy in Tehran, for their support.

The measurement of cosmogenic nuclide concentrations, performed at the ASTER AMS national facility (CEREGE, Aix en Provence), are supported by the INSU/CNRS, the French Ministry of Research and Higher Education, IRD and CEA. E; the ASTER team are acknowledged for the measurements (M. Arnold, G. Aumaître, K. Keddadouche). We thank G. Axen, B. Guest and P. Ballato for insightful comments on an earlier version of this manuscript and K. Hessami Azar, an anonymous reviewer, and an Associate Editor for helpful and constructive reviews. The Editor Onno Oncken is acknowledged for help and handling the manuscript. A. Walpersdorf and A. Landgraf are acknowledged for discussions on GPS-derived velocities in NE Iran, and denudation rates in central Alborz, respectively. The general government of Khorassan-e Razavi has efficiently helped us during two field works in 2005 and 2006.

References

Afshar Harb, A. (1979), The stratigraphy, tectonics and petroleum geology of the Kopeh Dagh region, northeastern Iran, PhD thesis, Pet. Geol. Sect., R. Sch. of Mines, Imp. Coll. of Sci. and Technol., London.

Aghanabati, A. (1986), Geological quadrangle map of Iran, Mashhad sheet, scale 1:250,000, 1 sheet, Geol. Surv. of Iran, Tehran.

Alavi, M. (1992), Thrust tectonics of the Binalood region, NE Iran, *Tectonics*, *11*(2), 360–370, doi:10.1029/91TC02217.

Arnold, M., S. Merchel, D. L. Bourlès, R. Braucher, L. Benedetti, R. C. Finkel, G. Aumaître, A. Gottdang, and M. Klein (2010), The French Accelerator Mass Spectrometry Facility ASTER: Improved performance and developments, *Nucl. Instrum. Methods Phys. Res., Sect. B*, *268*, 1954–1959, doi:10.1016/j.nimb.2010.02.107.

Authemayou, C., O. Bellier, D. Chardon, L. Benedetti, Z. Malekzade, C. Claude, B. Angeletti, E. Shabanian, and M. R. Abbassi (2009), Quaternary slip-rates of the Kazerun and the Main Recent Faults: active strike-slip partitioning in the Zagros fold-and-thrust belt, *Geophys. J. Int.*, *178*, 524–540, doi:10.1111/j.1365-246X.2009.04191.x.

Axen, G. J., P. J. Lam, M. Grove, D. F. Stockli, and J. Hassanzadeh (2001), Exhumation of the west central Alborz mountains, Iran, Caspian subsidence, and collision-related tectonics, *Geology*, *29*, 559–562, doi:10.1130/0091-7613(2001)029b0559:EOTWCAN2.0.CO;2.

Ballato, P., C. E. Uba, A. Landgraf, M. R. Strecker, M. Sudo, D. F. Stockli, A. Friedrich, and S. H. Tabatabaei (2011), Arabia-Eurasia continental collision: Insights from late Tertiary foreland-basin evolution in the Alborz Mountains, northern Iran, *Geol. Soc. Am. Bull.*, *123*(1–2), 106–131, doi:10.1130/B30091.1.

Berberian, M. (1983), The southern Caspian: a compressional depression floored by a trapped, modified oceanic crust, *Can. J. Earth Sci.*, *20*, 163–183, doi:10.1139/e83-015.

Berberian, M., and G. C. P. King (1981), Towards a paleogeography and tectonic evolution of Iran, *Can. J. Earth Sci.*, *18*, 210–265, doi:10.1139/e81-019.

Berberian, M., and R. Yeats (1999), Patterns of historical earthquake rupture in the Iranian Plateau, *Bull. Seismol. Soc. Am.*, *89*, 120–139.

Bierman, P. R. (1994), Using in situ produced cosmogenic isotopes to estimate rates of landscape evolution: A review from the geomorphic perspective, *J. Geophys. Res.*, *99*(B7), 13,885–13,896, doi:10.1029/94JB00459.

Braucher, R., S. Merchel, J. Borgomano, and D. L. Bourlès (2011), Production of cosmogenic radionuclides at great depth: A multi element approach, *Earth Planet. Sci. Lett.*, *309*(1–2), 1–9, doi:10.1016/j.epsl.2011.06.036.

Brown, E. T., J. M. Edmond, G. M. Raisbeck, F. Yiou, M. D. Kurz, and E. J. Brook (1991), Examination of surface exposure ages of Antarctic moraines using in-situ produced ^{10}Be and ^{26}Al, *Geochim. Cosmochim. Acta*, *55*, 2269–2283, doi:10.1016/0016-7037(91)90103-C.

Bullard, T. F., and W. R. Lettis (1993), Quaternary fold deformation associated with blind thrust faulting, Los Angeles basin: California, *J. Geophys. Res.*, *98*(B5), 8349–8369, doi:10.1029/93JB00012.

Chmeleff, J., F. Blanckenburg, K. Kossert, and D. Jakob (2010), Determination of the ^{10}Be half-life by multicollector ICP-MS and liquid scintillation counting, *Nucl. Instrum. Methods Phys. Res., Sect. B*, *268*(2), 192–199, doi:10.1016/j.nimb.2009.09.012.

Cooke, R. U., A. Warren, and A. Goudie (1993), *Desert Geomorphology*, UCL Press, London.

Davis, D., J. Suppe, and F. Dahlen (1983), Mechanics of fold-and-thrust belts and accretionary wedges, *J. Geophys. Res.*, *88*(B2), 1153–1172, doi:10.1029/JB088iB02p01153.

Deino, A., and R. Potts (1992), Age-probability spectra from examination of single-crystal ^{40}Ar/^{39}Ar dating results: Examples from Olorgesailie, southern Kenya Rift, *Quat. Int.*, *13–14*, 47–53, doi:10.1016/1040-6182(92)90009-Q.

Djamali, M., H. Akhani, R. Khoshravesh, V. Andrieu-Ponel, P. Ponel, and S. Brewer (2011), Application of the Global Bioclimatic Classification to Iran: implications for understanding the modern vegetation and biogeography, *Ecol. Mediter.*, *37*(1), 91–114.

Djamour, Y., et al. (2010), GPS and gravity constraints on continental deformation in the Alborz mountain range, Iran, *Geophys. J. Int.*, *183*(3), 1287–1301, doi:10.1111/j.1365-246X.2010.04811.x.

Dunaï, T. J. (2010), *Cosmogenic Nuclides: Principles, Concepts and Applications in the Earth Surface Sciences*, Cambridge Univ. Press, New York.

Dunne, J., D. Elmore, and P. Muzikar (1999), Scaling factors for the rates of production of cosmogenic nuclides for geometric shielding and attenuation at depth on sloped surfaces, *Geomorphology*, *27*(1-2), 3–11, doi:10.1016/S0169-555X(98)00086-5.

Farbod, Y., O. Bellier, E. Shabanian, and M. R. Abbassi (2011), Geomorphic and structural variations along the Doruneh Fault System (central Iran), *Tectonics*, *30*, TC6014, doi:10.1029/2011TC002889.

Farr, T. G., et al. (2007), The Shuttle Radar Topography Mission, *Rev. Geophys.*, *45*, RG2004, doi:10.1029/2005RG000183.

Ghaemi, F., F. Ghaemi, and K. Hosseini (1999), Geological map of Iran, Neyshabur sheet-7762, scale 1:100,000, 1 sheet, Geol. Surv. of Iran, Tehran.

Gosse, J. C., and F. M. Phillips (2001), Terrestrial in situ cosmogenic nuclides: Theory and application, *Quat. Sci. Rev.*, *20*, 1475–1560, doi:10.1016/S0277-3791(00)00171-2.

Guest, B., B. K. Horton, G. J. Axen, J. Hassanzadeh, and W. C. McIntosh (2007), Middle to late Cenozoic basin evolution in the western Alborz Mountains: Implications for the onset of collisional deformation in northern Iran, *Tectonics*, *26*, TC6011, doi:10.1029/2006TC002091.

Hollingsworth, J., J. Jackson, R. Walker, M. R. Gheitanchi, and M. J. Bolourchi (2006), Strike-slip faulting, rotation and along-strike elongation in the Kopeh Dagh Mountains, NE Iran, *Geophys. J. Int.*, *166*, 1161–1177, doi:10.1111/j.1365-246X.2006.02983.x.

Hollingsworth, J., M. Fattahi, R. Walker, M. Talebian, A. Bahroudi, M. J. Bolourchi, J. Jackson, and A. Copley (2010), Oroclinal bending, distributed thrust and strike-slip faulting, and the accommodation of Arabia–Eurasia convergence in NE Iran since the Oligocene, *Geophys. J. Int.*, *181*, 1214–1246, doi:10.1111/j.1365-246X.2010.04591.x.

Javidfakhr, B., O. Bellier, E. Shabanian, S. Ahmadian, and A. Saidi (2011a), Plio-Quaternary tectonic regime changes in the transition zone between Alborz and Kopeh Dagh mountain ranges (NE Iran), *Tectonophysics*, *506*, 86–108, doi:10.1016/j.tecto.2011.04.013.

Javidfakhr, B., O. Bellier, E. Shabanian, L. Siame, L. Léanni, D. Bourlès, and S. Ahmadian (2011b), Fault kinematics and active tectonics at the southeastern boundary of the eastern Alborz (Abr and Khij Fault Zones): Geodynamic implications for NNE Iran, *J. Geodyn.*, *52*, 290–303, doi:10.1016/j.jog.2011.02.005.

Keller, E. A., D. B. Seaver, D. L. Laduzinsky, D. L. Johnson, and T. L. Ku (2000), Tectonic geomorphology of active folding over buried reverse faults: San Emigdio Mountain front, southern San Joaquin Valley, California, *Geol. Soc. Am. Bull.*, *112*(1), 86–97, doi:10.1130/0016-7606(2000)112<86:TGOAFO>2.0.CO;2.

Korschinek, G., et al. (2010), A new value for the half-life of ^{10}Be by heavy-ion elastic recoil detection and liquid scintillation counting, *Nucl. Instrum. Methods Phys. Res., Sect. B*, *268*(2), 187–191, doi:10.1016/j.nimb.2009.09.020.

Lal, D. (1991), Cosmic ray labeling of erosion surfaces: in-situ nuclide production rates and erosion models, *Earth Planet. Sci. Lett.*, *104*, 424–439, doi:10.1016/0012-821X(91)90220-C.

Landgraf, A. (2010), Fault interaction at different time- and length scales: The North Tehran Thrust and Mosha-Fasham Fault (Alborz mountains, Iran), PhD thesis, Potsdam Univ., Potsdam, Germany.

Le Béon, M., Y. Klinger, M. Al-Qaryouti, A. S. Mériaux, R. C. Finkel, A. Elias, O. Mayyas, F. J. Ryerson, and P. Tapponnier (2010), Early Holocene and late Pleistocene slip rates of the southern Dead Sea Fault determined from ^{10}Be cosmogenic dating of offset alluvial deposits, *J. Geophys. Res.*, *115*, B11414, doi:10.1029/2009JB007198.

Le Dortz, K., et al. (2009), Holocene right-slip rate determined by cosmogenic and OSL dating on the Anar fault, Central Iran, *Geophys. J. Int.*, *179*(2), 700–710, doi:10.1111/j.1365-246X.2009.04309.x.

Le Dortz, K., et al. (2011), Dating inset terraces and offset fans along the Dehshir Fault (Iran) combining cosmogenic and OSL methods, *Geophys. J. Int.*, *185*, 1147–1174, doi:10.1111/j.1365-246X.2011.05010.x.

Lowell, T. V. (1995), The application of radiocarbon age estimates to the dating of glacial sequences: an example from the Miami sublobe, Ohio, USA, *Quat. Sci. Rev.*, *14*, 85–99, doi:10.1016/0277-3791(94)00113-P.

Lyberis, N., and G. Manby (1999), Oblique to orthogonal convergence across the Turan block in the post-Miocene, *AAPG Bull.*, *83*(7), 1135–1160.

Majidi, B. (1978), Etude petrostructurale de la région de Mashhad, Iran: Les problèmes des métamorphites, serpentinites, et granitoïdes hercyniens, PhD thesis, 274 pp., Univ. Sci. et Méd. de Grenoble, Grenoble, France.

Masson, F., M. Anvari, Y. Djamour, A. Walpersdorf, F. Tavakoli, M. Daignières, H. Nankali, and S. Van Gorp (2007), Large-scale velocity

field and strain tensor in Iran inferred from GPS measurements: New insight for the present-day deformation pattern within NE Iran, *Geophys. J. Int.*, *170*, 436–440, doi:10.1111/j.1365-246X.2007.03477.x.

McClusky, S., R. Reilinger, S. Mahmoud, D. Ben Sari, and A. Tealeb (2003), GPS constraints on Africa (Nubia) and Arabia plate motions, *Geophys. J. Int.*, *155*(1), 126–138, doi:10.1046/j.1365-246X.2003.02023.x.

Merchel, S., and U. Herpers (1999), An update on radiochemical separation techniques for the determination of long-lived radionuclides via accelerator mass spectrometry, *Radiochim. Acta*, *84*, 215–219.

Merchel, S., M. Arnold, G. Aumaître, L. Benedetti, D. L. Bourlès, R. Braucher, V. Alfimov, S. P. H. T. Freeman, P. Steier, and A. Wallner (2008), Towards more precise ^{10}Be and ^{36}Cl data from measurements at the 10^{-14} level: Influence of sample preparation, *Nucl. Instrum. Methods Phys. Res., Sect. B*, *266*(22), 4921–4926, doi:10.1016/j.nimb.2008.07.031.

Meyer, B., and K. Le Dortz (2007), Strike-slip kinematics in central and eastern Iran: Estimating fault slip rates averaged over the Holocene, *Tectonics*, *26*, TC5009, doi:10.1029/2006TC002073.

Namson, J., and T. L. Davis (1988), Seismically active fold and thrust belt in the San Joaquin Valley, central California, *Geol. Soc. Am. Bull.*, *100*, 257–273, doi:10.1130/0016-7606(1988)100<0257:SAFATB>2.3.CO;2.

Nishiizumi, K., M. Imamura, M. W. Caffee, J. R. Southon, R. C. Finkel, and J. McAninch (2007), Absolute calibration of ^{10}Be AMS standards, *Nucl. Instrum. Methods Phys. Res., Sect. B*, *258*, 403–413, doi:10.1016/j.nimb.2007.01.297.

Phillips, F. M., M. G. Zreda, J. C. Gosse, J. Klein, E. B. Evenson, R. D. Hall, O. A. Chadwick, and P. Sharma (1997), Cosmogenic ^{36}Cl and ^{10}Be ages of Quaternary glacial and fluvial deposits of the Wind River Range, Wyoming, *Geol. Soc. Am. Bull.*, *109*(11), 1453–1463, doi:10.1130/0016-7606(1997)109<1453:CCABAO>2.3.CO;2.

Pourlatifi, A., M. Alavi-Naini, N. Shojai, M. Vedige, M. Bahremand, F. Ariai, and V. Javadi (2001), Geological map of Iran, Torqabeh sheet-7862, scale 1:100,000, 1 sheet, Geol. Surv. of Iran, Tehran.

Regard, V., O. Bellier, J. C. Thomas, M. R. Abbassi, J. L. Mercier, E. Shabanian, K. Feghhi, and S. Soleymani (2004), Accommodation of Arabia-Eurasia convergence in the Zagros-Makran transfer zone, SE Iran, A transition between collision and subduction through a young deforming system, *Tectonics*, *23*, TC4007, doi:10.1029/2003TC001599.

Regard, V., O. Bellier, R. Braucher, F. Gasse, D. Bourlès, J. Mercier, J. C. Thomas, M. R. Abbassi, E. Shabanian, and S. Soleymani (2006), ^{10}Be dating of alluvial deposits from southeastern Iran (the Hormoz Strait area), *Palaeogeogr. Palaeoclimatol. Palaeoecol.*, *242*, 36–53, doi:10.1016/j.palaeo.2006.05.012.

Reilinger, R., et al. (2006), GPS constraints on continental deformation in the Africa-Arabia-Eurasia continental collision zone and implications for the dynamics of plate interactions, *J. Geophys. Res.*, *111*, B05411, doi:10.1029/2005JB004051.

Ritz, J. F., R. Vassallo, R. Braucher, E. T. Brown, S. Carretier, and D. L. Bourlès (2006a), Using in situ–produced ^{10}Be to quantify active tectonics in the Gurvan Bogd mountain range (Gobi-Altay, Mongolia), in *Application of Cosmogenic Nuclides to the Study of Earth Surface Processes: The Practice and the Potential*, edited by L. L. Siame, D. L. Bourlès, and E. T. Brown, *Spec. Pap. Geol. Soc. Am.*, *415*, 87–110.

Ritz, J.-F., H. Nazari, R. Salamati, A. Shafeii, S. Solaymani, and P. Vernant (2006b), Active transtension inside central Alborz: A new insight into the northern Iran–southern Caspian geodynamics, *Geology*, *34*, 477–480, doi:10.1130/G22319.1.

Schmidt, S., R. Hetzel, J. Kuhlmann, F. Mingorance, and V. A. Ramos (2011), A note of caution on the use of boulders for exposure dating of depositional surfaces, *Earth Planet. Sci. Lett.*, *302*, 60–70, doi:10.1016/j.epsl.2010.11.039.

Sella, G. F., T. H. Dixon, and A. Mao (2002), REVEL: A model for recent plate velocities from space geodesy, *J. Geophys. Res.*, *107*(B4), 2081, doi:10.1029/2000JB000033.

Shabanian, E. (2009), Active tectonic study in northeast Iran: contribution of the Kopeh Dagh and Binalud mountains to the accommodation of the Arabia-Eurasia convergence, PhD thesis, Paul Cezanne Univ., Aix-en-Provence, France. [Available at http://tel.archives-ouvertes.fr/tel-00433264/fr/.]

Shabanian, E., L. Siame, O. Bellier, L. Benedetti, and M. R. Abbassi (2009a), Quaternary slip-rates along the north-eastern boundary of the Arabia-Eurasia collision zone (Kopeh Dagh Mountains, north-east Iran), *Geophys. J. Int.*, *178*, 1055–1077, doi:10.1111/j.1365-246X.2009.04183.x.

Shabanian, E., O. Bellier, L. Siame, N. Arnaud, M. R. Abbassi, and J. J. Cochemé (2009b), New tectonic configuration in NE Iran: Active strike-slip faulting between the Kopeh Dagh and Binalud mountains, *Tectonics*, *28*, TC5002, doi:10.1029/2008TC002444.

Shabanian, E., O. Bellier, M. R. Abbassi, L. L. Siame, and Y. Farbod (2010), Plio-Quaternary stress states in NE Iran: Kopeh Dagh and Allah Dagh-Binalud mountains, *Tectonophysics*, *480*, 280–304, doi:10.1016/j.tecto.2009.10.022.

Shabanian, E., V. Acocella, A. Gioncada, H. Ghasemi, and O. Bellier (2012), Structural control on volcanism in intraplate post collisional settings: Late Cenozoic to Quaternary examples of Iran and eastern Turkey, *Tectonics*, *31*, TC3013, doi:10.1029/2011TC003042.

Sheikholeslami, M. R., and M. Kouhpeyma (2012), Structural analysis and tectonic evolution of the eastern Binalud Mountains, NE Iran, *J. Geodyn.*, *61*, 23–46, doi:10.1016/j.jog.2012.06.010.

Siame, L. L., E. Shabanian, and O. Bellier (2009), Extrusion tectonics and subduction in the eastern South Caspian region since 10 Ma: COMMENT, *Geology*, *37*(12), 197–198, doi:10.1130/G25701C.1.

Stöcklin, J. (1974), Northern Iran: Alborz Mountains, in *Mesozoic–Cenozoic Belts*, edited by A. M. Spencer, *Geol. Soc. Spec. Publ.*, *4*, 213–234.

Stone, J. O. H. (2000), Air pressure and cosmogenic isotope production, *J. Geophys. Res.*, *105*, 23,753–23,759, doi:10.1029/2000JB900181.

Tavakoli, F. (2007), Present-day kinematics of the Zagros and east of Iran faults, PhD thesis, Univ. of Joseph Fourier, Grenoble, France. [Available at http://tel.archives-ouvertes.fr/tel-00285919/fr/.]

Taylor, J. R. (1997), *An Introduction to Error Analysis, The Study of Uncertainties in Physical Measurements*, 2nd ed., Univ. Sci. Books, Sausalito, Calif., doi:10.1063/1.882103.

Tchalenko, J. S. (1975), Seismicity and structure of the Kopet Dagh (Iran, USSR), *Philos. Trans. R. Soc. London, Ser. A*, *278*, 1–28, doi:10.1098/rsta.1975.0019.

Thomas, D. S. G. (1989), *Arid Zone Geomorphology*, Halsted, New York.

Tirrul, R., I. R. Bell, R. J. Griffis, and V. E. Camp (1983), The Sistan suture zone of eastern Iran, *Geol. Soc. Am. Bull.*, *94*, 134–150, doi:10.1130/0016-7606(1983)94<134:TSSZOE>2.0.CO;2.

Troeh, F. R. (1965), Landform equations fitted to contour maps, *Am. J. Sci.*, *263*, 616–627, doi:10.2475/ajs.263.7.616.

Vernant, P., et al. (2004), Present-day crustal deformation and plate kinematics in the Middle East constrained by GPS measurements in Iran and northern Oman, *Geophys. J. Int.*, *157*(1), 381–398, doi:10.1111/j.1365-246X.2004.02222.x.

Walker, R., and J. Jackson (2004), Active tectonics and Late Cenozoic strain distribution in central and eastern Iran, *Tectonics*, *23*, TC5010, doi:10.1029/2003TC001529.

Wells, S. G., L. D. McFadden, J. Poths, and C. T. Olinger (1995), Cosmogenic ^{3}He exposure dating of stone pavements: implications for landscape evolution in deserts, *Geology*, *23*, 613–616, doi:10.1130/0091-7613(1995)023<0613:CHSEDO>2.3.CO;2.

Yeats, R. S. (1986), Active faults related to folding, in *Active Tectonics*, edited by E. Keller and N. Pinter, pp. 63–79, Natl. Acad. Press, Washington, D. C.

Zanchi, A., F. Berra, M. Mattei, M. R. Ghassemi, and J. Sabouri (2006), Inversion tectonics in central Alborz, Iran, *J. Struct. Geol.*, *20*, 1–15.

Zreda, M. G., F. M. Phillips, and D. Elmore (1994), Cosmogenic ^{36}Cl accumulation in unstable landforms, 2. Simulations and measurements on eroding moraines, *Water Resour. Res.*, *30*, 3127–3136, doi:10.1029/94WR00760.